J. Appl. Comput. Mech., xx(x) (2026) 1-23
DOI: 10.22055/jacm.2026.49306.5879

ISSN: 2383-4536
jacm.scu.ac.ir

Shahid Chamran University of Ahvaz

Journal of Applied and Computational Mechanics

Research Paper

Comparative Assessment of Hyperelastic Models for Simulating Mechanical Hysteresis in Synthetic Yarns for Offshore Mooring

Daniel Magalhães da Cruz, Felipe Tempel Stumpf, Jakson Manfredini Vassoler

Applied Mechanics Group (GMAp), Graduate Program in Mechanical Engineering (PROMEC), Federal University of Rio Grande do Sul (UFRGS), 425, Sarmento Leite Street, Porto Alegre, 90050-170, Brazil, Email: daniel.cruz@ufrgs.br (D.M.C.); felipe.stumpf@ufrgs.br (F.T.S.); jmvassoler@ufrgs.br (J.M.V.)

Received April 23 2026; Revised September 03 2026; Accepted for publication September 04 2026.
✉ Corresponding author: D.M. da Cruz (daniel.cruz@ufrgs.br & dacruz.daniel@hotmail.com)

Abstract. Synthetic fibers are widely employed in offshore mooring systems due to their high specific strength, low weight, corrosion resistance, and favorable fatigue performance. However, their mechanical response under cyclic loading is complex, involving nonlinear elasticity, viscoelasticity, energy dissipation, stiffness evolution, and load-history dependence. Reliable constitutive models are therefore essential for predictive analysis and design. This study presents a systematic comparative assessment of phenomenological hyperelastic strain energy models for simulating mechanical hysteresis in synthetic yarns. The constitutive framework combines finite deformations, incompressibility, and viscoelastic memory through an internal variable, with model parameters identified by constrained numerical optimization using stabilized experimental hysteresis curves as reference data. Seven fiber classes were investigated: aramid, high-modulus polyethylene (HMPE), low-creep HMPE, liquid crystal polymer (LCP), polyamide (PA), polyester (PET), and high-elongation polyester (HE PET). Twenty strain energy models were evaluated under the same computational framework, resulting in 140 material-model combinations. The simulations reproduced the experimental hysteresis responses with good overall consistency, yielding a global mean error of 3.325%. Stumpf-Marczak provided the best global performance, followed by Davies-De-Thomas, Yeoh Modified, and Bechir-Boufala-Chevalier. Aramid and LCP presented the lowest material mean errors, whereas PA exhibited the highest, associated with its more complex stress–strain curvature changes during cycling. The results demonstrate that model selection depends on the material response and that greater mathematical complexity does not necessarily ensure better fitting. The study provides an exploratory comparative baseline for constitutive model selection and highlights the need to balance fitting accuracy, numerical robustness, and computational effort in offshore mooring applications.

Keywords: Cyclic behavior, Hyperelastic models, Synthetic fibers, Continuum mechanics, Parameter optimization, Strain energy function.

1. Introduction

Advancements in deepwater and ultra-deepwater offshore operations have driven the development and adoption of mooring systems based on synthetic fibers, which have progressively replaced traditional steel solutions due to their high strength-to-weight ratio, lower density, and superior performance under severe environmental conditions [1-4]. Materials such as polyester (polyethylene terephthalate, PET), polyamide (PA), aramid, and high-modulus polyethylene (HMPE) are widely used in anchoring applications and offshore operations, providing mechanical performance compatible with the demanding operational requirements of these structures [2, 5, 6].

However, the mechanical behavior of these fibers is intrinsically complex, being governed by material and geometric nonlinearities, as well as time-dependent effects and load-history dependence [7, 8]. Under cyclic loading conditions, which are typical of offshore mooring systems, phenomena such as mechanical hysteresis, energy dissipation, structural accommodation, stiffness evolution, and the accumulation of residual strains emerge [9-12]. These characteristics are directly associated with the viscoelastic nature of polymeric materials, whose response depends not only on the instantaneous strain state, but also on the previously imposed loading path [13].

In this context, predicting the stress–strain behavior of these fibers through purely analytical approaches becomes impractical, especially when large deformations and nonlinear effects are significant [14, 15]. Therefore, phenomenological models and numerical simulation play a central role in the analysis and prediction of mechanical behavior, allowing the incorporation of a consistent mathematical and computational framework capable of reproducing the experimentally observed response [16, 17].

Among the different available approaches, phenomenological constitutive models based on strain energy functions stand out, being widely used to describe polymeric and composite materials under large deformations [18-21]. These models are formulated within the framework of continuum mechanics, based on tensorial descriptions of the strain and stress states, allowing a consistent representation of the nonlinear material behavior [22]. In general, for polymers, such models are expressed as functions of the deformation tensor invariants, with the invariants I_1 and I_2 being the most commonly used in the construction of strain energy functions, since the incompressibility hypothesis is usually adopted, which implies neglecting the volumetric invariant I_3 [23-25].

Published online: September 18 2026

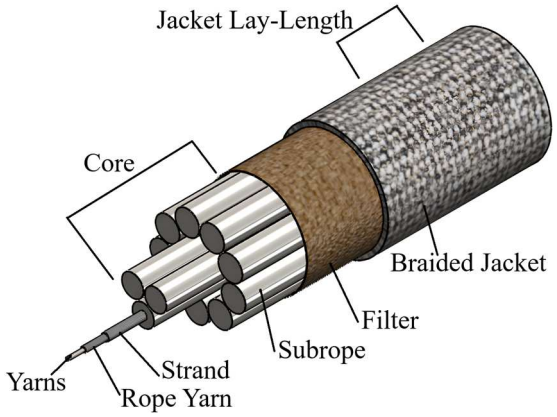

Fig. 1. Schematic structure of an offshore mooring rope [26].

This study is conducted at the structural level of synthetic multifilaments (yarns), which constitute the basic unit for the manufacture of offshore mooring ropes, as schematically illustrated in Fig. 1. The selection of this level of analysis allows a more direct evaluation of the intrinsic properties of the polymeric material, minimizing the influence of constructional effects present at higher structural levels, such as twist angle, braid pitch, void ratio, number of strands, and rope or braid geometric configurations. In this way, the analyzed mechanical response is predominantly associated with the constitutive behavior of the material, enabling a more consistent calibration of the hyperelastic models.

The choice of the strain energy function directly influences the ability of the model to represent the mechanical response of the material, especially under cyclic loading conditions, and different formulations may lead to significant variations in the quality of fit to the experimental data [27]. In this sense, the identification of constitutive parameters through numerical optimization techniques becomes a fundamental step, allowing the calibration of the models in order to minimize the error between the simulated response and the reference experimental data.

The methodological developments that support the present work are part of a continuous line of research focused on the constitutive modeling of synthetic fibers through formulations based on continuum mechanics and tensorial descriptions coupled with strain energy functions. The initial development of this numerical code dates back to an undergraduate study [28], in which a first simulation framework for dynamic cycling in HMPE and PET fibers was proposed, considering three hyperelastic models, although still with an inefficient parameter optimization approach. Subsequently, Stumpf et al. [29] expanded the application of the Stumpf-Marczak model to simulate the cyclic behavior of four different fibers and one sub-rope, ensuring physical consistency through compliance with the Baker-Ericksen inequalities. Later, da Cruz et al. [30] and Stumpf et al. [31] advanced the modeling of hybrid systems by analyzing the behavior of multi-material lines arranged in series and composed of HMPE and PET, demonstrating the constitutive representation capability of these configurations using the three-term Yeoh model [30], and the Stumpf-Marczak model with a single set of parameters for different configurations [31]. In da Cruz et al. [32], an evaluation of seven different strain energy functions applied to polyester was conducted, establishing that the modified Yeoh model provided the best performance in terms of mean error. The evolution of the methodology also included the analysis of different construction levels, ranging from multifilaments to mooring sub-ropes [33], as well as its extension to multiple loading regimes, including rupture, creep, and cyclic loading in HMPE and PET fibers [34], which later enabled constitutive numerical simulations for creep rupture tests in low-creep HMPE fibers [35]. Another recent study focused on mathematical formulations, incorporating different mathematical terms and dependencies on the invariants I_1 and I_2, including additive linear, quadratic, cubic, and exponential terms, for the simulation of dynamic cycles in synthetic fibers [36]. In addition, investigations on cycle-by-cycle behavior made it possible to correlate stiffness evolution with the numerical response of the models, assigning physical meaning to phenomenological parameters [37], while subsequent studies demonstrated the relationship between mechanical hysteresis stabilization, stiffness stabilization, and convergence of the mean simulation error [38]. Finally, recent approaches have also explored the simulation of dynamic cycles with progressive loading amplitudes, extending the applicability of the model to conditions with variable amplitudes [39]. This body of contributions demonstrates the continuous development and robustness of the numerical tool employed, culminating in the comprehensive approach proposed in the present study.

Despite the advances in the constitutive modeling of synthetic fibers, a large portion of the available studies remain focused on specific materials, limited sets of models, or particular loading conditions. In addition, many approaches do not comprehensively investigate the ability of the models to represent stabilized mechanical hysteresis under cyclic loading, a condition of great relevance for offshore applications. Therefore, a significant gap remains regarding the systematic and comparative evaluation of the performance of different strain energy models when applied to multiple materials under equivalent conditions, particularly with respect to identifying the most suitable model for different synthetic fibers.

In this context, the present work proposes a systematic comparative assessment of phenomenological hyperelastic strain energy models for simulating the mechanical hysteresis behavior of synthetic yarns used in offshore mooring systems. The methodology combines a tensorial formulation consistent with continuum mechanics, viscoelastic memory represented through an internal variable, and numerical parameter identification based on stabilized experimental hysteresis curves. Twenty strain energy models are evaluated for seven classes of synthetic fibers under the same experimental reference, tensorial framework, optimization procedure, objective function, and error criterion, resulting in 140 material–model combinations.

The original contribution of this study lies not in the proposition of a new strain energy function or optimization algorithm, but in the systematic investigation of how different mathematical structures of phenomenological hyperelastic models perform when embedded within the same viscoelastic tensorial framework and applied to synthetic yarns exhibiting markedly different mechanical responses. Previous studies have generally focused on specific materials, individual constitutive formulations, or limited sets of loading conditions, whereas the present approach provides a unified basis for examining the influence of the strain energy function on the representation of stabilized mechanical hysteresis across multiple fiber classes. Particular attention is given to differences in fitting capability among materials and models, the influence of constitutive complexity, the behavior of the identified parameters, and the practical balance between fitting accuracy and computational effort.

Table 1. Results for initial mechanical characterization and information, all fibers.

Property/Information	Aramid	HMPE	LC HMPE	LCP	PA	PET	HE PET
Linear density [tex]	168.95	181.22	164.51	174.01	284.52	227.33	232.91
Break force, or YBL [N]	355.20	560.73	480.70	361.20	212.96	182.47	171.44
Break elongation [mm]	17.01	14.90	19.42	15.92	93.48	66.15	84.23
Linear tenacity [N/tex]	2.10	3.09	2.92	2.08	0.75	0.80	0.74
Break strain [%]	3.40	2.98	3.88	3.18	18.70	13.23	16.85
Break stress [MPa]	3048.55	3001.37	2834.40	2906.06	853.29	1107.64	1015.81
Specific mass [g/cm^3]	1.45	0.97	0.97	1.40	1.14	1.38	1.38
Specific cost [U$/kg]	39.00	17.50	28.70	35.00	9.50	3.00	3.60

Because the evaluated strain energy models contain different numbers of adjustable parameters and different mathematical structures, the comparison is not intended to establish an absolute or universal ranking of constitutive formulations. Instead, the study provides an exploratory comparative baseline under a consistent calibration framework, allowing the relative fitting performance and numerical behavior of each model to be examined across different synthetic fibers. The results are intended to support constitutive model selection for subsequent numerical applications and to identify relevant directions for further investigations involving parameter sensitivity, model complexity, optimization strategies, and computational efficiency, contributing to the development of more reliable predictive tools for the design and analysis of mooring systems.

2. Materials and Methods

2.1. Fiber information and mechanical characterization

The synthetic fibers analyzed in this study comprise seven materials used in offshore mooring and operational applications: aramid, high-modulus polyethylene (HMPE), low-creep high-modulus polyethylene (LC HMPE), liquid crystal polymer (LCP), polyamide (PA), polyester (PET), and high-elongation polyester (HE PET). All specimens were extracted from virgin spools of untwisted multifilaments to ensure that the measured mechanical properties are directly associated with intrinsic material behavior, without the influence of constructional effects arising from higher-level manufacturing processes. Although the identification of specific product codes and manufacturers cannot be disclosed due to confidentiality agreements, it is relevant to note that the HMPE, LC HMPE, PET, and HE PET fibers are of Asian manufacture, whereas the aramid, LCP, and PA fibers are of European manufacture.

The initial mechanical characterization of the fibers was carried out to establish reference parameters for the subsequent dynamic tests and for the calibration of the numerical models. The tests were performed in accordance with recognized technical standards, with the linear density determined according to ASTM D1577 [40], while the rupture test (Yarn Break Load, YBL) was obtained in accordance with ISO 2062 [41] using specimens with an effective gauge length of 500 mm. Based on these results, the linear tenacity of the fibers was also determined as the ratio between breaking load and linear density. All tests were conducted under controlled environmental conditions, as specified by ISO 139 [42], ensuring consistency and reproducibility of the experimental data.

The results of the initial characterization are presented in Table 1, including linear density, rupture force (YBL), rupture elongation, and linear tenacity for each material. In addition, complementary properties relevant for analysis, modeling, and comparison are reported, such as conversion to stress and strain, the material density of the fibers, and the estimated specific cost. These parameters are essential both for interpreting mechanical behavior and for contextualizing offshore engineering applications, where mechanical performance and economic feasibility are decisive factors.

Data acquisition in the mechanical tests is performed in terms of force and elongation (or extension), both for the rupture tests and for the dynamic experiments. However, to ensure compatibility with the constitutive formulation based on continuum mechanics, it is necessary to express the results in terms of stress and strain. Considering the difficulty associated with the accurate determination of the cross-sectional area of yarns (bundle multifilament), an alternative approach is adopted for stress calculation:

$$\sigma = \frac{F \times \rho}{\rho_L} \tag{1}$$

where the stress (σ) is obtained from the experimentally measured force (F) in newtons, combined with the material specific mass (ρ) in grams per cubic centimeter and the linear density (ρ_L) of the fiber in grams per meter, allowing the determination of consistent stress values in megapascal. This approach ensures dimensional consistency and enables the direct use of experimental data in the calibration of the hyperelastic models.

The rupture stress values reported in Table 1 are obtained using Eq. (1). Figure 2(a) presents the rupture test results, showing the force–extension behavior directly obtained from the experimental test, whereas Fig. 2(b) presents the corresponding curve in terms of stress–strain after data conversion through Eq. (1). This transformation is equally applied to the data obtained from the dynamic tests, ensuring consistency between the quantities used in the numerical modeling and in the experimental validation.

This initial characterization stage therefore constitutes the experimental basis required for the execution of the dynamic tests and the subsequent constitutive simulations proposed in this study, since the dynamic test is force-controlled at a percentage of the Yarn Break Load (YBL).

2.2. Dynamic experimental test for mechanical hysteresis

The dynamic tests were conducted to characterize the mechanical hysteresis behavior of the synthetic fibers under cyclic loading, providing the experimental basis for the calibration and validation of the constitutive models. The tests were performed using an Instron ElectroPuls® E3000 servo-hydraulic machine operating under force control, suitable for high-precision dynamic testing of polymeric materials.

The specimens, consisting of multifilaments extracted from spools, were tested with an effective gauge length of 250 mm. The applied loading consisted of a sequence of 100 complete loading–unloading cycles with a sinusoidal waveform and a fixed frequency of 0.1 Hz, allowing the evaluation of the evolution of the mechanical behavior from the initial cycles to the stabilization of the dynamic response.

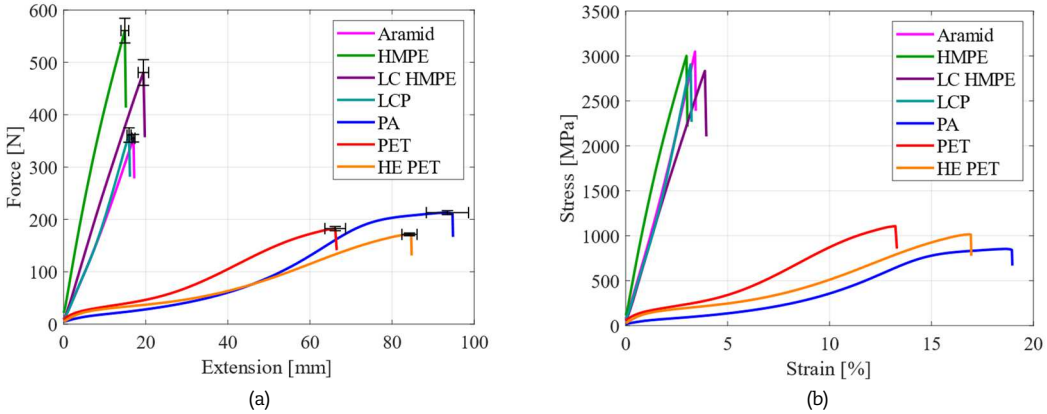

Fig. 2. Rupture results, all fibers, (a) Experimental force–extension, (b) Transformed stress–strain.

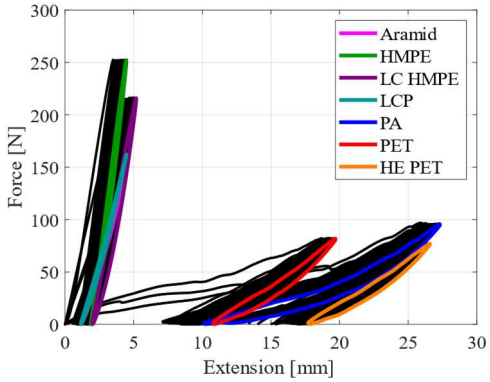

Fig. 3. Experimental force–extension response under cyclic loading, all fibers.

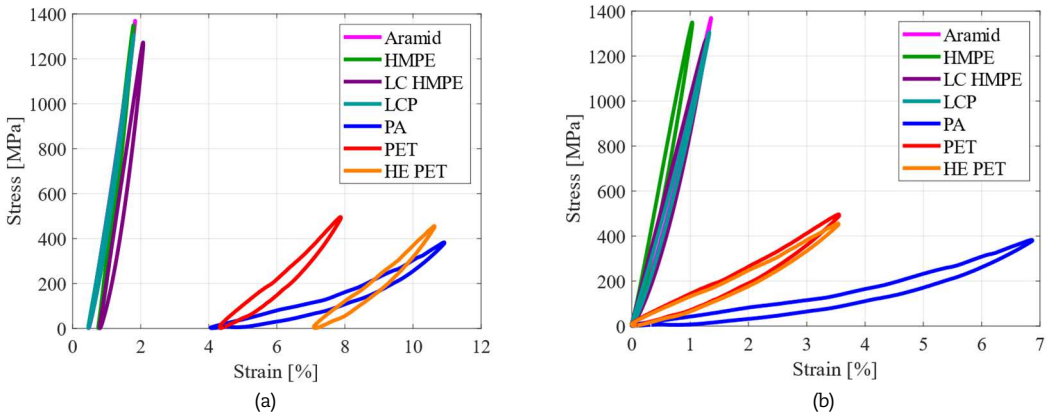

Fig. 4. Stress–strain curve (100th cycle), all fibers, (a) Real absolute values of strain, (b) Adjusted to zero strain.

The loading amplitude was individually defined for each material based on its respective breaking load (Yarn Break Load, YBL), previously determined during the mechanical characterization stage (Table 1). In all cases, the load range was established between 0 and 45% of the fiber YBL, ensuring a sufficiently high loading level to induce relevant viscoelastic effects, such as energy dissipation, structural accommodation, and stiffness evolution, without causing rupture during the test.

The tests were conducted in a controlled environment in accordance with ISO 139 [42]. During the experiments, force, elongation, and time data were continuously acquired, allowing the complete reconstruction of the mechanical hysteresis curves of each fiber throughout the 100 cycles.

Analogously to the procedure adopted in the initial characterization, the experimental data obtained in terms of force and extension were subsequently converted into stress and strain. Stress was determined using Eq. (1), allowing the results to be expressed in megapascal and ensuring compatibility with the tensorial formulation employed in the constitutive modeling.

For the numerical simulation stage, the 100th loading cycle is adopted as the reference, as it represents the mechanical hysteresis behavior under a more stabilized condition. This choice is justified by the reduction of transient effects typically observed in the initial cycles, in which structural accommodation mechanisms and internal adjustments of the viscoelastic response still predominate [38]. Therefore, the selected cycle provides a more consistent basis for the calibration and comparison of the different strain energy models evaluated in this study.

Figure 3 presents the experimental behavior obtained from dynamic tests in terms of force and extension throughout the 100 applied cycles. The evolution of the mechanical response with the number of cycles can be observed, with emphasis on the 100th cycle (colored), in which the response is already in a condition close to stabilization. This behavior highlights the initial effects of structural accommodation followed by the subsequent stabilization of mechanical hysteresis.

The experimental curve acquired in terms of force and extension is post-processed into stress and strain, considering the stabilized cycle. Figure 4(a) presents the stress–strain curve corresponding to the 100th cycle, obtained from the conversion of the experimental data through Eq. (1). Subsequently, Fig. 4(b) shows the same curve adjusted to start at zero strain, a procedure adopted to ensure compatibility with the implementation of the tensorial model and with the definition of the initial conditions of the numerical simulation.

The 100th cycles adjusted to the origin and presented in Fig. 4(b) for each fiber are adopted as the experimental reference for the constitutive numerical simulations through parametric optimization of the formulation and the strain energy models. Therefore, the established dynamic test provides the experimental basis required for the comparative analysis between experimental and numerical responses, allowing the evaluation of the ability of hyperelastic models to consistently reproduce the shape of the mechanical hysteresis curves of the different synthetic fibers investigated.

2.3. Continuum mechanics: Tensor mathematical model

The constitutive numerical simulation developed in this study is based on the finite strain formulation of continuum mechanics following the framework proposed by Simo and Hughes [43], employing a tensorial description to represent the nonlinear and load-history-dependent behavior of synthetic multifilaments. The adopted approach is phenomenological and combines a hyperelastic formulation, associated with the strain energy function (W), with a viscoelastic treatment through an internal variable, allowing an adequate representation of the mechanical hysteresis behavior observed experimentally. The material is assumed to be homogeneous, isotropic, and incompressible. The numerical code was developed in the MathWorks Inc. MATLAB® platform, similarly to previous studies reported in the literature [34, 36]. The specific expressions of the strain energy functions evaluated in this study are presented separately in Section 2.4.

Considering a body $\Omega \subset \mathbb{R}^3$ subjected to a finite deformation $\varphi: \Omega \to \mathbb{R}^3$, the deformation gradient ($\mathbf{F}$) is defined as:

$$\mathbf{F} = \frac{\partial \varphi(\mathbf{X})}{\partial \mathbf{X}} = \frac{\partial \mathbf{x}}{\partial \mathbf{X}} \tag{2}$$

where $\mathbf{X}$ represents the position of a material point in the reference (undeformed) configuration, and $\mathbf{x}$ is the corresponding position in the deformed configuration. The Jacobian of the transformation, $J = \det \mathbf{F} > 0$, measures the local volume change associated with the deformation.

The adopted formulation employs the multiplicative decomposition of Flory [44] to separate the deformation gradient ($\mathbf{F}$), as:

$$\mathbf{F} = \widehat{\mathbf{F}}\ \overline{\mathbf{F}} \tag{3}$$

where into a volumetric part ($\widehat{\mathbf{F}}$) and an isochoric part ($\overline{\mathbf{F}}$).

The volumetric and isochoric parts are defined, respectively, by:

$$\widehat{\mathbf{F}} = J^{1/3}\mathbf{I}, \text{ with } \det \widehat{\mathbf{F}} = \det \mathbf{F} = J \tag{4}$$

$$\overline{\mathbf{F}} = J^{-1/3}\mathbf{F}, \text{ with } \det \overline{\mathbf{F}} = 1 \tag{5}$$

where $\mathbf{I}$ is the identity tensor, $\mathbf{F}$ is the deformation gradient, and the determinant is indicated for each part, volumetric in Eq. (4) and isochoric in Eq. (5).

A real body (Ω) undergoing finite deformation (φ) stores energy, and this stored quantity is expressed through a strain energy density function (W), as given in:

$$W = W^{\text{vol}} + W^{\text{iso}} \tag{6}$$

where W^{vol} and W^{iso} denote the volumetric and isochoric contributions, respectively. Although the strain energy function is treated as a separate topic and will be presented in Section 2.4, particularly due to the extent and number of models considered, its introduction is important for mathematical development. This is because, for incompressible and nearly incompressible materials, the volumetric contribution W^{vol} vanishes, resulting only in isochoric terms:

$$W = W^{\text{iso}} = W(\bar{\mathbf{C}}) \tag{7}$$

where $\bar{\mathbf{C}}$ is the Cauchy-Green tensor for the isochoric part, which directly affects the tensorial formulation of the numerical code.

From the deformation gradient, the right Cauchy-Green tensor ($\mathbf{C}$) is defined as:

$$\mathbf{C} = \mathbf{F}^T\mathbf{F} \tag{8}$$

where $\mathbf{F}$ is the deformation gradient, and $\mathbf{F}^T$ is the transpose of the deformation gradient.

The modified form associated with the isochoric part ($\bar{\mathbf{C}}$), as given as:

$$\bar{\mathbf{C}} = \overline{\mathbf{F}}^T\overline{\mathbf{F}} = J^{-2/3}\mathbf{C} \tag{9}$$

where $\overline{\mathbf{F}}$ is the deformation gradient in isochoric part, and $\overline{\mathbf{F}}^T$ is the transpose of the deformation gradient in isochoric part.

The continuum mechanics invariants associated with the tensor $\bar{\mathbf{C}}$ are introduced:

$$\overline{I_1} = \text{tr}(\bar{\mathbf{C}}) \tag{10}$$

$$\overline{I_2} = \frac{1}{2}[\text{tr}(\bar{\mathbf{C}})^2 - \text{tr}(\bar{\mathbf{C}}^2)] \tag{11}$$

$$\overline{I_3} = \det(\bar{\mathbf{C}}) \tag{12}$$

where in Eq. (10) is defined for the first invariant in isochoric terms $\overline{I_1}$ as a trace operation on the right Cauchy-Green tensor in isochoric terms, in Eq. (11) for the second invariant in isochoric terms $\overline{I_2}$ as half the difference between the squared trace of the right Cauchy-Green deformation tensor in isochoric terms and the trace of the squared tensor in isochoric terms, and in Eq. (12) for the third invariant in isochoric terms $\overline{I_3}$ as the determinant of the right Cauchy-Green tensor in isochoric terms. Since the adopted

formulation employs the isochoric part of the deformation, these invariants are the ones effectively used in the constitutive construction of the model.

In the present study, the incompressibility hypothesis is adopted, which is a widely used approximation for polymeric materials. Under this assumption, the third invariant is unitary, $\overline{I_3} = \det(\bar{\mathbf{C}}) = 1$, so that the volumetric contribution is no longer relevant for the constitutive modeling employed herein. Consequently, the strain energy functions considered in this study are formulated only in terms of $\overline{I_1}$ and $\overline{I_2}$. Although the rigorous formulation is derived from the invariants of the isochoric part, for notational simplicity Section 2.4 represents these dependencies directly as $W(I_1)$ or $W(I_1, I_2)$.

The energy stored by the material is described by a scalar strain energy function (W), whose contribution to the second Piola-Kirchhoff stress tensor, in the isochoric part, is presented as:

$$\bar{\mathbf{S}} = 2\left(\frac{\partial W}{\partial \bar{I}_1} + \bar{I}_1 \frac{\partial W}{\partial \bar{I}_2}\right)\mathbf{I} - 2\frac{\partial W}{\partial \bar{I}_2}\bar{\mathbf{C}} + 2\bar{I}_3 \frac{\partial W}{\partial \bar{I}_3}\bar{\mathbf{C}}^{-1} \tag{13}$$

in this expression, W generically represents the adopted strain energy function, whose specific form depends on the hyperelastic model considered. Since the incompressibility hypothesis eliminates the need for a volumetric contribution, the practical formulation adopted in the present study remains governed by the terms associated with I_1 and I_2.

To represent the time-dependent effects and load-history dependence, an internal variable $\mathbf{H}$ is introduced, associated with the viscoelastic memory of the material. Its incremental update is given by:

$$\mathbf{H}_{n+1} = \exp\left(-\frac{\Delta t_n}{\tau}\right)\mathbf{H}_n + \exp\left(-\frac{\Delta t_n}{2\tau}\right)(\bar{\mathbf{S}}^{\circ}_{n+1} - \bar{\mathbf{S}}^{\circ}_{n}) \tag{14}$$

where Δt_n is the time increment between steps n and $n+1$, τ is the relaxation parameter of the model, and $\bar{\mathbf{S}}_n$ and $\bar{\mathbf{S}}_{n+1}$ are the isochoric stress tensors at consecutive steps.

To ensure that only the deviatoric contribution of the tensors is used in the final composition of the response, the deviatoric operator is employed, indicated by the superscript "$\circ$", also present in Eq. (14). The deviatoric operation is defined as:

$$\begin{aligned} \blacksquare^{\circ}_{n} &= \mathrm{DEV}_n(\blacksquare) = \blacksquare - \frac{1}{3}[\blacksquare : \mathbf{C}_n]\mathbf{C}_n^{-1} \\ \blacksquare^{\circ}_{n+1} &= \mathrm{DEV}_{n+1}(\blacksquare) = \blacksquare - \frac{1}{3}[\blacksquare : \mathbf{C}_{n+1}]\mathbf{C}_{n+1}^{-1} \end{aligned} \tag{15}$$

where the inner product $[\blacksquare : \mathbf{C}]$ corresponds to the double tensor contraction. In the presented expression, $\blacksquare$ denotes a generic tensor, which in the adopted constitutive formulation will be assigned to the internal variable ($\mathbf{H}$), and to the second Piola-Kirchoff stress tensor in isochoric terms ($\bar{\mathbf{S}}$).

The deviatoric functions associated with the system stiffness model, second Piola-Kirchhoff stress tensor and the internal variable provide the final stress matrix presented as:

$$\mathbf{S}_{\text{final}} = (1-\gamma)\mathrm{DEV}_{n+1}(\bar{\mathbf{S}}_{n+1}) + \gamma\mathrm{DEV}_{n+1}(\mathbf{H}_{n+1}) = (1-\gamma)\bar{\mathbf{S}}^{\circ}_{n+1} + \gamma\mathbf{H}^{\circ}_{n+1} \tag{16}$$

which includes the relative contribution between the instantaneous response and the portion associated with viscoelastic memory. In this expression, γ corresponds to a proportional stiffness parameter of the tensorial viscoelastic model.

Since direct comparison with the second Piola-Kirchhoff stress tensor is not convenient for the experimental data considered, the standard push-forward transformation is performed, yielding the spatial Kirchhoff stress tensor, as given:

$$\boldsymbol{\sigma}_{n+1} = \mathbf{F}_{n+1}\mathbf{S}_{\text{final}}\mathbf{F}^{T}_{n+1} \tag{17}$$

where $\boldsymbol{\sigma}$ is the spatial stress tensor, $\mathbf{F}$ is the deformation gradient, $\mathbf{F}^T$ is the transpose of the deformation gradient, and $\mathbf{S}_{\text{final}}$ is final stress matrix.

From Eq. (17), numerical stresses are obtained through the formulation for each strain energy model, which can then be compared with the experimental stress results. By defining n control points along the experimental mechanical hysteresis stress–strain curve, the same points can also be considered on the numerical curve, allowing the calculation of a point-by-point relative difference whose mean absolute value indicates the mean error (ϵ) of the numerical simulation with respect to the reference, as shown:

$$\epsilon[\%] = \frac{1}{n}\sum_{i=1}^{n}\left|\frac{\sigma_{\exp_i} - \sigma_{\text{num}_i}}{\sigma_{\exp_i}}\right| \times 100 \tag{18}$$

where $\sigma_{\exp_i}$ denotes the experimental reference stress and σ_{num_i} denotes the numerical stress obtained for the i-th evaluation point, while n represents the total number of points considered in the analysis.

The parameter ϵ presented in Eq. (18) is the criterion adopted in this study to quantify the fitting quality of each constitutive simulation. Lower values of ϵ indicate greater agreement between the numerical curve and the experimental curve, allowing a consistent comparison of the performance of the different strain energy models and the different material–model combinations analyzed.

In the presented formulation, it is important to emphasize that, in Eq. (14), the parameter τ is associated with the material relaxation time scale and, therefore, with the viscoelastic character of the response. Likewise, in Eq. (16), the parameter γ represents a stiffness fraction of the model, weighing the relative contribution to the response. These parameters must be distinguished from the constants C_n of the strain energy models, which will be presented in Section 2.4 and control the mathematical form of the function W. In other words, τ and γ belong to the viscoelastic tensorial framework of the constitutive formulation, whereas the constants C_n belong to the specific hyperelastic model adopted.

In the MATLAB® code implementation, model calibration and optimization of the formulation are performed through parametric optimization by minimizing the sum of the squared differences between the experimental stresses and the simulated stresses, where the simulated stresses depend on the parameters to be optimized. Thus, the objective function (p), formulated as a minimization problem, is defined according to:

$$\min_{\{\gamma,\tau,C_i\}} p = \sum_{k=1}^{N}[\sigma_{\exp}(\varepsilon_k) - \sigma_{\text{num}}(\varepsilon_k;\{\gamma,\tau,C_i\})]^2 \tag{19}$$

where σ_{exp} and σ_{num} are the experimental and numerical stresses corresponding to the strain ε_k, and $\{\gamma, \tau, C_i\}$ are the parameters to be adjusted with respect to the tensorial formulation (γ and τ) and the strain energy model (C_n).

The optimization procedure was carried out through constrained local nonlinear optimization using the MATLAB® fmincon solver with the interior-point algorithm [45]. For all material–model combinations, the optimization was initialized from a null parameter vector, while model-dependent lower and upper bounds were prescribed for the adjustable parameters whenever required. Each material–model combination was independently optimized once using the same initialization criterion, resulting in 140 optimization procedures for the results reported in this study. The optimization settings included a maximum of $100{,}000$ function evaluations and $100{,}000$ iterations, with the function tolerance set to 10^{-6}. None of the reported simulations terminated upon reaching the prescribed limits on function evaluations or iterations; instead, termination occurred according to the convergence criteria of the optimization algorithm. The same optimization procedure was consistently applied throughout the complete dataset to provide a unified calibration framework. Because fmincon is a local optimization solver, the identified parameter sets correspond to converged solutions within the adopted initialization and parameter bounds and are not guaranteed to represent global minima. Accordingly, the present study focuses on the relative fitting performance of the evaluated strain energy models under a consistent and computationally feasible optimization procedure.

In this way, the formulation presented in this subsection establishes the general tensorial framework of the constitutive model employed, incorporating finite deformations, the assumptions of homogeneity, isotropy, and incompressibility, viscoelastic memory, and parametric identification through numerical optimization. With this basis established, the following subsection presents the specific expressions of the strain energy functions W used in the comparative study.

2.4. Hyperelastic strain energy models

The strain energy function has already been introduced as a fundamental element in the determination of the second Piola-Kirchhoff stress tensor, as presented in Eq. (13). Within the framework of continuum mechanics, hyperelastic models are generally the most suitable for highly deformable elastic materials, such as polymers and synthetic yarns, since they establish a constitutive relationship based on the energy stored in the material during the deformation process [46]. A hyperelastic material, or Green elastic material, according to Truesdell and Noll [47] and Beatty [48], postulates the existence of a specific strain energy function W, also referred to as Helmholtz free energy, which may be described for homogeneous and isotropic materials in terms of the invariants, i.e., $W(I_1, I_2, I_3)$. For incompressible and nearly incompressible materials, an assumption adopted in the present formulation, the strain energy functions are described exclusively in terms of I_1 and I_2.

The choice of the functional form of W directly influences the ability of the model to represent the mechanical behavior of the material, especially under cyclic loading conditions with the presence of hysteresis. Different hyperelastic models exhibit distinct mathematical structures and invariant dependencies, resulting in different levels of flexibility for fitting the experimental data, as well as lower or higher computational effort.

With the objective of comprehensively evaluating the performance of these formulations, the present study considers a set of twenty strain energy models widely reported in the literature. These models include classical formulations, as well as extensions with different levels of mathematical complexity. Table 2 presents the models considered, their respective mathematical expressions for the strain energy function (W), and the corresponding references.

Table 2. Hyperelastic strain energy models considered in this study.

Model	Mathematical Expression	Reference(s)
Amin	$W = C_1(I_1-3) + \left(\frac{C_2}{C_4+1}\right)(I_1-3)^{C_4+1} + \left(\frac{C_3}{C_5+1}\right)(I_1-3)^{C_5+1}$	[49]
Bechir-Boufala-Chevalier	$W = C_1(I_1-3) + C_2(I_2-3) + C_3(I_1-3)^2 + C_4(I_2-3)^2 + C_5(I_1-3)^3$	[50]
Davies-De-Thomas	$W = \left(\frac{C_1}{2\left(1-\frac{C_2}{2}\right)}\right)(I_1-3+C_3^2)^{1-\frac{C_2}{2}} + C_4(I_1-3)^2$	[51]
Gent-Thomas	$W = C_1(I_1-3) + 3C_2\ln(I_2)$	[52]
Hartmann-Neff 3 terms	$W = C_1(I_1^3-27) + C_2(I_1-3) + C_3\left(I_2^{3/2}-\sqrt{27}\right)$	[53]
Hartmann-Neff 5 terms	$W = C_1(I_1^3-27) + C_2(I_1-3) + C_3(I_1-3)^2 + C_4\left(I_2^{3/2}-\sqrt{27}\right) + C_5\left(I_2^{3/2}-\sqrt{27}\right)^2$	[53]
Hartmann-Neff 7 terms	$W = C_1(I_1^3-27) + C_2(I_1-3) + C_3(I_1-3)^2 + C_4(I_1-3)^3 + C_5\left(I_2^{3/2}-\sqrt{27}\right) + C_6\left(I_2^{3/2}-\sqrt{27}\right)^2 + C_7\left(I_2^{3/2}-\sqrt{27}\right)^3$	[53]
Humphrey-Yin	$W = C_1(\exp(C_2(I_1-3))-1)$	[54]
Knowles	$W = \frac{C_1}{2C_2}\left(\left(1+\frac{C_2(I_1-3)}{C_3}\right)^{C_3}-1\right)$	[55]
Mooney-Rivlin 2 terms	$W = C_1(I_1-3) + C_2(I_2-3)$	[56, 57]
Mooney-Rivlin 3 terms	$W = C_1(I_1-3) + C_2(I_2-3) + C_3(I_1-3)(I_2-3)$	[56, 57]
Mooney-Rivlin 5 terms	$W = C_1(I_1-3) + C_2(I_2-3) + C_3(I_1-3)(I_2-3) + C_4(I_1-3)^2 + C_5(I_2-3)^2$	[56, 57]
Neo-Hooke	$W = C_1(I_1-3)$	[58]
Stumpf-Marczak	$W = \frac{C_1}{C_2}(1-\exp(-C_2(I_1-3))) + \frac{C_5}{2C_3}\left(\left(1+\frac{C_3(I_1-3)}{C_4}\right)^{C_4}-1\right) + C_6 I_2\ln\left(\frac{I_2}{3}\right)$	[59]
Veronda-Westmann	$W = C_1(\exp(C_3(I_1-3))-1) - C_2(I_2-3)$	[60]
Yamashita-Kawabata	$W = C_1(I_1-3) + \frac{C_2}{C_3+1}(I_1-3)^{C_3+1}$	[61]
Yeoh 2 terms	$W = C_1(I_1-3) + C_2(I_1-3)^2$	[62]
Yeoh 3 terms	$W = C_1(I_1-3) + C_2(I_1-3)^2 + C_3(I_1-3)^3$	[62]
Yeoh 5 terms	$W = C_1(I_1-3) + C_2(I_1-3)^2 + C_3(I_1-3)^3 + C_4(I_1-3)^4 + C_5(I_1-3)^5$	[62]
Yeoh Modified	$W = C_1(I_1-3) + C_2(I_1-3)^2 + C_3(I_1-3)^3 + \frac{C_4}{C_5}(1-\exp(-C_5(I_1-3)))$	[63]

After the definition of the strain energy functions, each model is incorporated into the tensorial formulation presented in Section 2.3, and its parameters are identified through the numerical optimization procedure given in Eq. (19). In this way, it becomes possible to consistently evaluate the ability of each model to reproduce the mechanical hysteresis behavior of the different fibers analyzed, considering both the shape of the stress–strain curves and the mean error associated with the simulation.

It should be emphasized that the invariant dependence adopted in the present study follows directly from the assumptions of homogeneity, isotropy, and incompressibility established in the constitutive formulation. Under these conditions, the strain energy functions are commonly expressed in terms of I_1 and I_2. However, for other classes of materials, compressible, anisotropic, or materials with preferred internal orientations, additional invariants such as I_3, I_4, I_5 and I_6 may be required to adequately represent the constitutive behavior of the material [64-67].

It is also important to note that hyperelastic strain energy models are commonly divided into phenomenological and micromechanical formulations. Phenomenological models are constructed from the observed macroscopic mechanical response of the material, seeking to reproduce experimental stress–strain behavior through invariant-based mathematical functions. In contrast, micromechanical models are derived from statistical or physical descriptions of the polymer network, incorporating molecular chain characteristics, bond mechanisms, or thermodynamic variables. In the present work, all models considered belong to the phenomenological category, which is consistent with the objective of comparatively evaluating their predictive capability based on experimental hysteresis curves.

3. Results and Discussion

Due to the extensive nature of the present study, involving the combination of seven materials and twenty strain energy models, the complete set of graphical results from the constitutive simulations was organized into appendices in order to preserve the clarity and fluency of the main discussion. The results corresponding to each material are presented in the following appendices: Appendix A for aramid, Appendix B for high-modulus polyethylene (HMPE), Appendix C for low-creep high-modulus polyethylene (LC HMPE), Appendix D for liquid crystal polymer (LCP), Appendix E for polyamide (PA), Appendix F for polyester (PET), and Appendix G for high-elongation polyester (HE PET).

This organization allows a detailed individual analysis of each material–model combination, while maintaining the focus of this section on the comparative results and the global trends observed.

By examining the complete set of numerical simulations for all materials and all strain energy models (Appendices A–G), it can be stated that, in general, the simulations exhibited good visual convergence with respect to the discrete experimental points shown in the graphs, except for a few cases that presented lower agreement. This makes it necessary to quantitatively assess the quality of the simulations through the mean error parameter ϵ, defined in Eq. (18).

Table 3 presents the mean error values obtained for all simulations performed. The results were organized to allow analyses by both material and model, including row means (overall performance of each model), column means (overall performance of each material), and the global mean of all simulations, highlighted in bold in the lower-right corner.

It is important to emphasize that the color map was applied to facilitate the comparative visualization of the results and was used consistently on a column-by-column basis, that is, individually for each material. Thus, in the gradient where green represents the lowest mean error and red represents the highest mean error, the interpretation should always be made within each column. Therefore, even when the absolute error values differ among materials, each column contains one green cell indicating the best numerical simulation and one red cell indicating the worst numerical simulation for that material. The only exception to this criterion occurs in the final row of material averages, in which the color map was applied horizontally considering only the values of that row.

The first aspect to be highlighted is the overall quality of the constitutive simulations. Visually, the graphs presented in Appendices A–G show good convergence between the numerical curves and the experimental points and, according to the adopted mathematical criterion, (with the exception of a group of models for polyamide), the vast majority of simulations exhibited low mean error ($< 5\%$). Considering the full set of evaluated cases, a global mean error of only 3.325% was obtained, as highlighted in bold in Table 3.

Table 3. Mean error of constitutive numerical simulations, all fibers and all models.

	Aramid	HMPE	LC HMPE	LCP	PA	PET	HE PET	Mean
Amin	1.589	2.548	2.829	2.452	6.576	2.785	3.145	3.132
Bechir-Boufala-Chevalier	0.644	2.188	2.370	1.428	6.685	2.546	3.223	2.726
Davies-De-Thomas	1.150	3.096	2.860	2.078	3.105	1.878	2.909	2.439
Gent-Thomas	1.271	3.165	3.454	2.199	9.752	3.310	3.226	3.768
Hartmann-Neff 3 terms	1.230	3.143	2.885	2.116	6.745	2.573	3.235	3.133
Hartmann-Neff 5 terms	0.837	3.106	2.340	1.860	5.352	3.526	4.704	3.104
Hartmann-Neff 7 terms	1.226	1.816	2.340	1.860	5.785	4.270	5.876	3.310
Humphrey-Yin	1.871	8.237	3.575	2.294	9.527	2.947	3.297	4.535
Knowles	1.753	3.097	2.855	2.241	9.752	5.144	6.682	4.503
Mooney-Rivlin 2 terms	1.210	3.165	3.454	2.142	9.752	3.310	3.226	3.751
Mooney-Rivlin 3 terms	1.210	3.161	3.454	1.969	9.752	3.310	3.226	3.726
Mooney-Rivlin 5 terms	1.210	1.949	2.370	1.905	11.303	7.250	3.235	4.175
Neo-Hooke	1.753	3.165	3.454	2.241	9.752	3.310	3.226	3.843
Stumpf-Marczak	1.096	1.124	1.871	2.056	4.103	1.966	2.106	2.046
Veronda-Westmann	1.923	2.941	2.667	2.317	4.900	2.448	3.336	2.933
Yamashita-Kawabata	1.753	3.096	2.860	2.241	6.573	2.565	3.150	3.177
Yeoh 2 terms	1.753	3.096	2.852	2.241	7.481	2.681	3.235	3.334
Yeoh 3 terms	1.753	3.096	2.863	2.241	6.685	2.546	3.223	3.201
Yeoh 5 terms	1.753	3.096	2.872	2.241	6.570	2.571	3.163	3.181
Yeoh Modified	1.144	3.096	2.863	2.074	3.512	2.139	2.532	2.480
Mean	1.407	3.069	2.854	2.110	7.183	3.154	3.498	**3.325**

Before comparing the numerical results, it is important to clarify the scope of the adopted performance criterion. The evaluated strain energy models differ in both mathematical structure and number of adjustable constants; therefore, the mean error should not be interpreted as an absolute measure of constitutive superiority. Models with greater parametric flexibility may possess an increased capability to reproduce experimental data, although a larger number of parameters does not necessarily result in lower fitting errors, as demonstrated by the results presented in Table 3. Accordingly, the comparisons discussed herein refer to the relative fitting performance obtained under the adopted experimental and computational framework. The mean error is therefore used as a consistent criterion for assessing the ability of each calibrated formulation to reproduce the experimental hysteresis curves, while model complexity, numerical robustness, parametric behavior, and computational effort are considered complementary aspects of the overall assessment. Furthermore, the global mean errors reported in Table 3 should be interpreted as descriptive aggregate measures of model performance across the seven investigated material classes rather than as indicators of statistical significance. Since these materials exhibit distinct mechanical responses and do not constitute statistical replicates of a common material population, the differences among the global mean errors are not used herein to establish statistically significant differences among the evaluated models. Instead, these values provide a comparative summary of fitting performance within the investigated dataset and should be interpreted together with the material-specific results.

In general, the mean errors vary among the models, highlighting the dependence of the numerical response on the functional form of the strain energy function W. Within the adopted calibration and evaluation framework, the mean errors varied among the models, highlighting the influence of the functional form of the strain energy function on the numerical response. The Stumpf-Marczak model presented the lowest global mean error (2.046%), followed by Davies-De-Thomas (2.439%), Modified Yeoh (2.480%), and Bechir-Boufala-Chevalier (2.726%). These results indicate that these formulations provided the most consistent fitting performance across the set of analyzed materials under the adopted optimization procedure. Conversely, Humphrey-Yin and Knowles presented global mean errors above 4.5%, indicating comparatively lower fitting capability within the same evaluation framework, although these errors remain relatively low in absolute terms. Importantly, these results should not be interpreted as evidence of universal superiority or inferiority among the constitutive models, since their mathematical structures and numbers of adjustable parameters differ.

The analysis by material shows that PA presents the highest material mean error (7.183%), indicating greater difficulty in reproducing its mechanical hysteresis response with the adopted phenomenological constitutive framework. This behavior may be associated with the pronounced changes in slope and curvature observed along its experimental stress–strain cycle, which impose additional challenges for the numerical representation. From a physical perspective, the comparatively complex response of PA may also reflect loading-history-dependent or microstructural mechanisms that are not explicitly represented by the adopted formulation. Possible contributions may include strain-induced structural rearrangements or crystallization, Mullins-type stress softening, and irreversible deformation associated with viscoplastic yielding, which could affect stiffness evolution and the shape of the hysteresis loop. However, the experimental methodology employed in this study was not designed to independently identify these mechanisms; therefore, their possible influence should be regarded as a hypothesis rather than a demonstrated explanation for the higher errors obtained for PA. In contrast, aramid presents the lowest material mean error (1.407%).

From the standpoint of mean error dispersion for each material across the simulations of the twenty strain energy models, LCP stands out for presenting the smallest variation between the best and worst model, of approximately 1%. In contrast, polyamide exhibited the largest variation between the best and worst performance, exceeding 8%.

A comparison among the investigated materials indicates that the differences in fitting performance are associated with the characteristics of their stabilized mechanical hysteresis responses. Aramid and LCP, which presented the lowest material mean errors of 1.407% and 2.110%, respectively, exhibited comparatively narrower hysteresis loops and more regular stress–strain trajectories, with smaller differences between the loading and unloading paths. These characteristics appear to facilitate their representation by different strain energy formulations, as also indicated by the relatively small dispersion of the errors obtained for LCP. In contrast, PA presented both the highest material mean error (7.183%) and the largest variation between the best and worst model performances. Its more pronounced changes in slope and curvature throughout the stress–strain cycle impose greater demands on the mathematical flexibility of the constitutive formulation. HMPE, LC HMPE, PET, and HE PET exhibited intermediate mean errors of 3.069%, 2.854%, 3.154%, and 3.498%, respectively, demonstrating that fitting performance cannot be attributed exclusively to a single material characteristic, such as elongation capacity or hysteresis magnitude. Overall, the results suggest that the ability of the adopted framework to represent each fiber depends on the complete shape of the stabilized hysteresis response and on how effectively the strain energy function accommodates changes in stiffness and curvature when coupled with the viscoelastic tensorial formulation.

For a more detailed analysis of model performance, as well as for an objective graphical presentation of the constitutive simulation results, the simulations corresponding to the best and worst fits were selected for each material based on the mean error values presented in Table 3. These results are graphically presented in Fig. 5–11, respectively for each material, allowing a direct comparison between the experimental and numerical responses, as well as between the best and worst performances among the models used in the constitutive simulations.

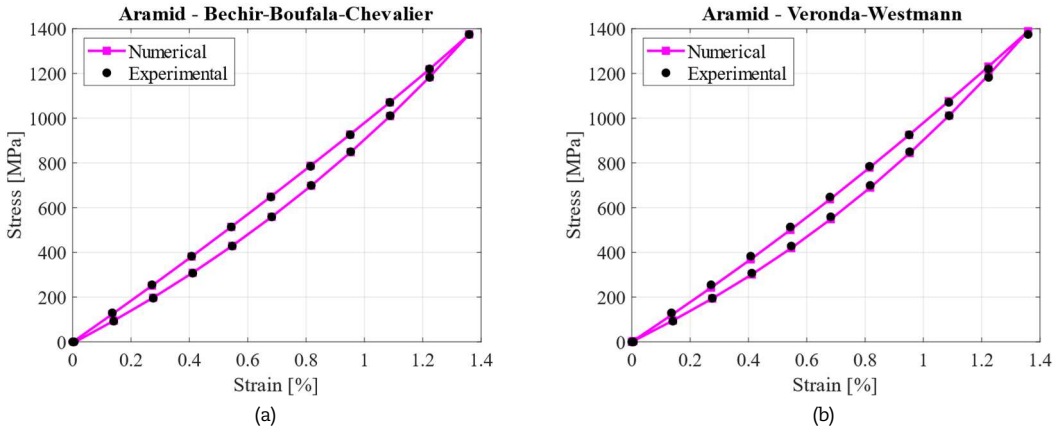

Fig. 5. Numerical stress–strain response, Aramid, (a) Best-performing model: $\epsilon = 0.644\%$, (b) Worst-performing model: $\epsilon = 1.923\%$.

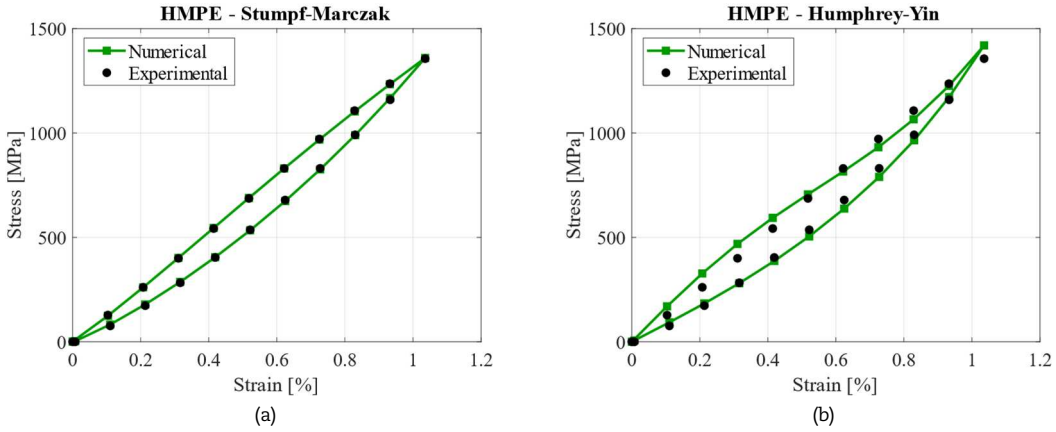

Fig. 6. Numerical stress–strain response, HMPE, Best-performing model: $\epsilon = 1.124\%$, (b) Worst-performing model: $\epsilon = 8.237\%$.

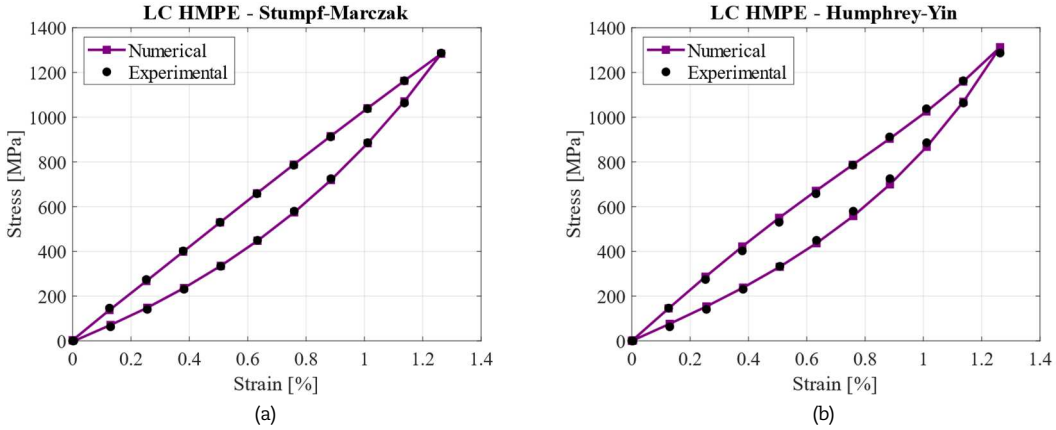

Fig. 7. Numerical stress–strain response, LC HMPE, (a) Best-performing model: $\epsilon = 1.871\%$, (b) Worst-performing model: $\epsilon = 3.575\%$.

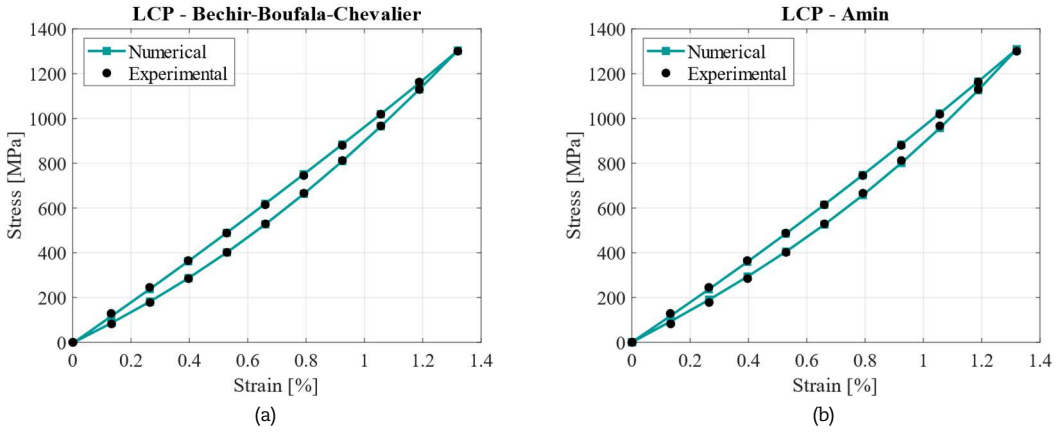

Fig. 8. Numerical stress–strain response, LCP, (a) Best-performing model: $\epsilon = 1.428\%$, (b) Worst-performing model: $\epsilon = 2.452\%$.

For the numerical simulations of aramid mechanical hysteresis, the Bechir-Boufala-Chevalier model provided the best performance, whereas the Veronda-Westmann model presented the worst performance among the tested models. Between the best and worst models for aramid (Fig. 5), no significant visual differences are observed, which is consistent with the low variation between the mean errors (< 1.3%). Any discrepancy in the "worst model" between the numerical and experimental responses can only be identified through careful observation of specific points in Fig. 5(b), due to the small, almost imperceptible, difference between the markers.

For the HMPE mechanical hysteresis cycle, the Stumpf-Marczak model provided the best performance, whereas the Humphrey-Yin model presented the worst performance among the tested models. For HMPE (Fig. 6), the worst model exhibits a visible and clearly identifiable divergence in the graph, altering the curvature specifically in the loading branch. In contrast, the best model shows excellent agreement between the discrete experimental control points and the numerical response.

For the LC HMPE fiber (Fig. 7), the best- and worst-performing models coincide with those observed for HMPE, with Stumpf-Marczak as the best model and Humphrey-Yin as the worst among the tested models. However, unlike the behavior observed for HMPE, the worst model in this case still presents good visual convergence between the experimental and numerical points. Any discrepancies in the "worst model" for LC HMPE can only be perceived through the small variation between the markers when compared with the graph corresponding to the best performance in the constitutive simulation.

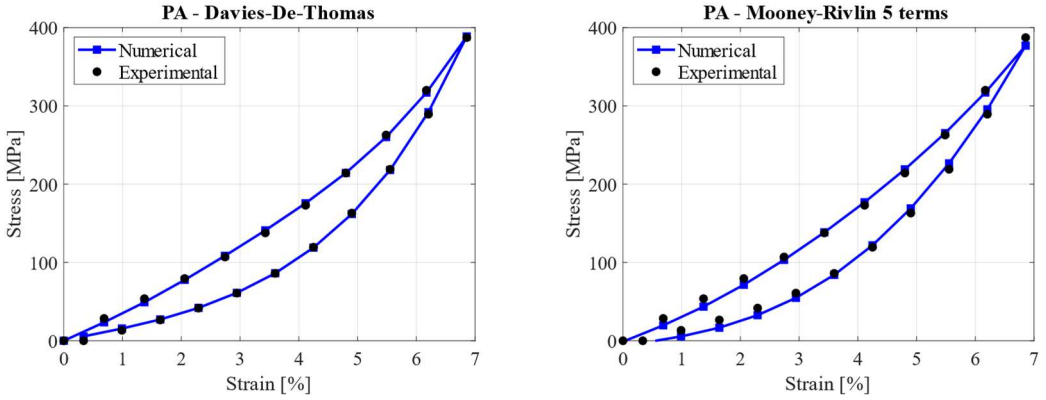

Fig. 9. Numerical stress–strain response, PA, (a) Best-performing model: $\epsilon = 3.105\%$, (b) Worst-performing model: $\epsilon = 11.303\%$.

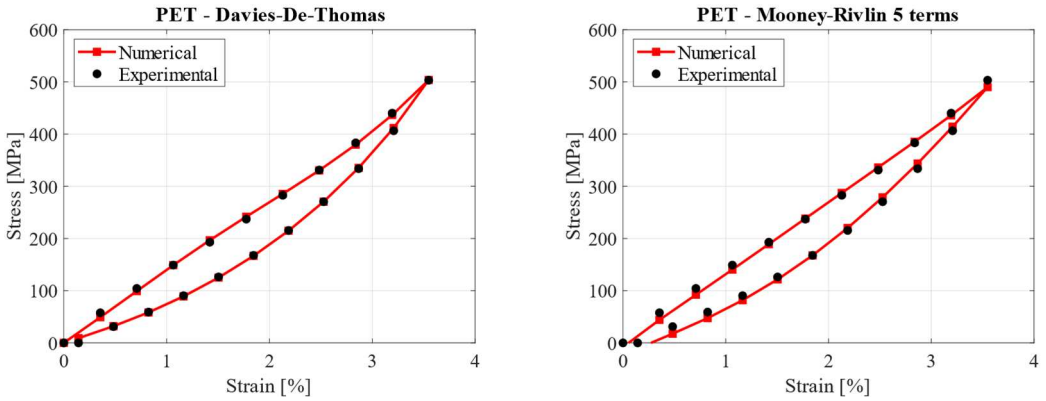

Fig. 10. Numerical stress–strain response, PET, (a) Best-performing model: $\epsilon = 1.878\%$, (b) Worst-performing model: $\epsilon = 7.250\%$.

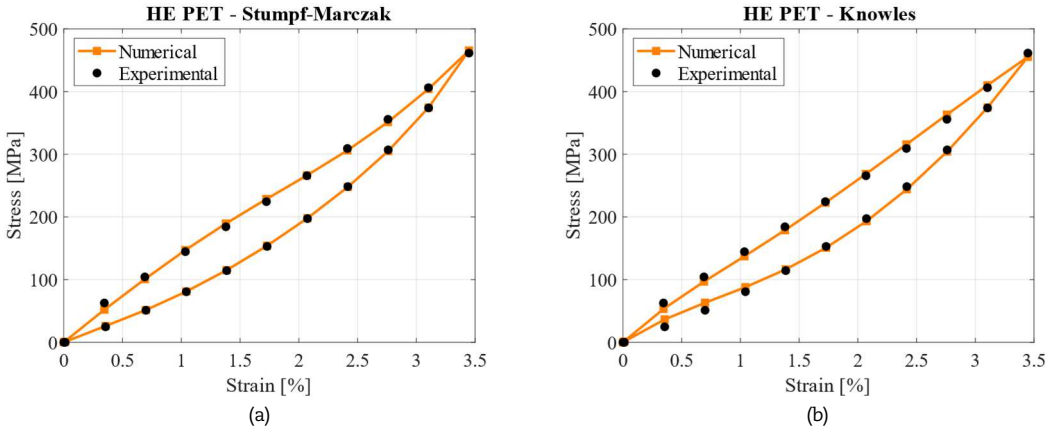

Fig. 11. Numerical stress–strain response, HE PET, (a) Best-performing model: $\epsilon = 2.106\%$, (b) Worst-performing model: $\epsilon = 6.682\%$.

The LCP fiber (Fig. 8) presents the smallest variation between the best and worst model performances among those tested, with the Bechir-Boufala-Chevalier model providing the best fit and the Amin model the worst performance. This small dispersion, in the order of approximately 1%, results in highly satisfactory graphical results, including for the complete set of simulations presented in Appendix D. Such a high level of convergence across different models may be interpreted as an indication of a constitutive response that is simpler to represent, possibly with a stronger predominance of elastic terms over viscous contributions. It is also observed that the hysteresis loop is narrower, or closer to a linear behavior, with a smaller difference between the loading and unloading branches, similarly to what is observed for aramid. This characteristic may help explain why these two fibers (aramid and LCP) exhibited some of the lowest global mean errors in the constitutive simulations (1.407% and 2.110%, respectively).

For the polyamide fiber (Fig. 9), the Davies-De-Thomas model presents the best performance, whereas the Mooney-Rivlin 5 terms model presents the worst performance among all evaluated models. In the latter case, the final numerical point is particularly noteworthy because the simulated stress becomes negative. It is important to consider the mathematical definition of the mean error adopted in this study, since significant deviations at low reference stress values may produce large individual contributions to the error summation due to the relative difference between experimental and numerical points, as defined in Eq. (18). This consideration does not eliminate the poor fitting performance of the model, which presents the highest mean error among all 140 simulations performed in this study (11.303%). Nevertheless, acceptable agreement can still be observed at higher stress levels, particularly for the points above 100 MPa in Fig. 9(b). From a constitutive perspective, the negative stress value may be associated

with the greater mathematical flexibility introduced by the higher-order polynomial terms and the coupled dependence on I_1 and I_2 in the Mooney-Rivlin 5 terms formulation. Because the optimization procedure minimizes the global discrepancy over the complete hysteresis cycle, the resulting parameter combination may provide an acceptable compromise among most experimental points while producing excessive local curvature near the end of the unloading path. Furthermore, the parameter bounds adopted in the optimization procedure do not explicitly impose convexity, monotonicity, or stability conditions throughout the complete deformation range. Consequently, the interaction among the polynomial terms may generate a locally non-physical continuation of the numerical response toward negative stress values.

For the polyester fiber (Fig. 10), the models presenting the best and worst performances coincide with those identified for PA, namely Davies-De-Thomas and Mooney-Rivlin 5 terms, respectively. In the latter simulation, a behavior similar to that observed for PA occurs, with the final numerical point reaching a negative stress value. The recurrence of this behavior for two different materials suggests that the non-physical local response may be associated with the interaction between the mathematical flexibility of the Mooney-Rivlin 5 terms formulation, the optimized parameter set, and the specific experimental hysteresis response, rather than being an isolated characteristic of a single material. Nevertheless, this localized deviation should be distinguished from the overall fitting capability of the model throughout the remaining portions of the mechanical hysteresis cycle.

For high-elongation polyester (Fig. 11), the best-performing model among those tested was the Stumpf-Marczak model, whereas the worst performance corresponded to the Knowles model. In the constitutive simulation obtained with the Knowles model (worst model), the penultimate point of the numerical curve, located in the unloading branch, is particularly noteworthy, as it produces a constriction in the curve shape and places the numerical point above the corresponding experimental reference point. Consequently, the simulated curve assumes a sharper shape in the region of lower stresses and strains (end of graph) when compared with the experimental behavior.

An additional observation should be made regarding the experimental control points adopted for each fiber. Although the 100th cycle was shifted to the origin, as indicated in Fig. 4(b), for operational reasons related to the execution of the code for all fibers without imposing an initial strain, the reference points remain consistent with the actual behavior of each material during the 100th cycle. In this context, it is observed that the initial loading point and the final unloading point, in terms of strain, are extremely similar for aramid, HMPE, LC HMPE, LCP, and HE PET. However, for polyamide and polyester, a certain difference between these strain values is observed. It is difficult to determine whether the applied loading produced any permanent damage or whether these distinct values would be recovered after a period of stress relaxation in the specimen. Nevertheless, it can be stated that the cycle was already stabilized, a condition verified for all materials through the cycle-by-cycle analysis of the stress–strain response, with all stabilizations occurring before the 50th cycle according to the adopted mathematical criterion. This subtle difference between the strain at the beginning of loading and at the end of unloading, observed for polyamide and polyester, represents an additional difficulty to be captured by the model, since the mechanical hysteresis simulation naturally tends to seek coincidence between the initial and final discrete points of the cycle.

Returning to the numerical simulations, in general, the best-performing models showed excellent ability to reproduce both the shape of the stress–strain curve and its slope throughout the cycle, during both loading and unloading, adequately reflecting the material stiffness and the energy dissipation associated with mechanical hysteresis. It is also observed that, for some materials, different models exhibit similar performances, suggesting that the additional complexity of certain formulations does not always result in a significant improvement in fitting quality. This behavior is particularly relevant when evaluating the balance between mathematical complexity and simulation accuracy.

The overall analysis of the results shows that the ability to represent mechanical hysteresis behavior is directly associated with the flexibility of the strain energy function. In general, models with a larger number of terms or with combined dependence on the invariants I_1 and I_2 tend to provide better performance, although this tendency is not universal. It is observed, for example, that the Bechir-Boufala-Chevalier and Stumpf-Marczak models, both dependent on I_1 and I_2, account for 5 out of the 7 simulations classified as the best performance for each material.

In addition, it is observed that the exclusive dependence on I_1, combined with mathematically simple expressions, as in Neo-Hooke- or Humphrey-Yin-type models, may be insufficient to adequately capture the response of some materials, especially those exhibiting more complex behavior, with changes in curvature and high elongation. On the other hand, the introduction of exponential terms or higher-order polynomial terms tends to contribute to a better adaptation of the numerical curve to the experimental response. This may help explain the strong global performance of the Stumpf-Marczak model, which depends on I_1 and I_2 and whose mathematical structure incorporates exponential, power-law, and logarithmic terms.

To some extent, the superior performance of numerical simulations involving formulations with simultaneous dependence on I_1 and I_2 had already been indicated in the literature [36]. Although this approach was not explored in the present study, it remains a relevant possibility for future investigations to consider the best-performing models identified herein and expand their phenomenological strain energy functions through the additive inclusion of terms originally dependent on I_1 also as functions of I_2, and vice versa. Naturally, such a strategy would increase the number of constants C_n associated with the model, approximately doubling the number of parameters adjusted. Nevertheless, this represents an important line of investigation, especially when comparing the increase in computational cost with the potential improvement in simulation quality.

Although the Stumpf-Marczak model presented high global performance for the set of analyzed materials, it is important to emphasize that the variability observed among the materials reinforces the need for a careful selection of the constitutive model, since there is no single formulation capable of representing all investigated materials with equal accuracy. Furthermore, although the present study adopts an extensive approach by considering twenty strain energy models, the literature still provides several other hyperelastic constitutive alternatives worthy of investigation.

In addition to the mean error evaluation, the parameters obtained through the numerical optimization process provide complementary information regarding the behavior of the constitutive formulation and the way in which each strain energy model fits the experimental data when coupled with the tensorial description. Appendix H presents, in a complete manner, the constants obtained from all constitutive numerical simulations performed, gathering the parameters γ and τ of the viscoelastic description, as well as the constants C_n associated with each strain energy model for all fibers.

However, the interpretation of these parameters must be carried out with caution. All models employed in this study are phenomenological in nature, so that the constants obtained through parametric optimization do not directly represent intrinsic chemical, physical, or mechanical properties of the materials or load cycle. Instead, these parameters reflect the best possible mathematical fit between the numerical response and the experimental mechanical hysteresis curve, while respecting the admissible bounds imposed on each constant according to each strain energy model. Therefore, the identified values should be primarily understood as constitutive fitting parameters rather than as quantities with direct material meaning.

Even so, some global trends can be highlighted. The parameter γ, associated in Eq. (16) with the relative weighting between the

instantaneous contribution of the second Piola-Kirchhoff stress tensor and the contribution of the viscoelastic internal variable in the composition of the final stress, assumed a value equal or very close to 0.50 in most simulations. This behavior suggests that, for most material–model combinations, the tensorial formulation converged toward an approximately balanced partition between the two components of the response. Although this result should not be interpreted as a universal property of the analyzed materials, it indicates a consistent tendency of the optimization routine toward a similar proportional distribution of the effective stiffness of the model.

On the other hand, the parameter τ, associated with the relaxation time scale of the viscoelastic formulation, proved to be significantly more sensitive to the combination of material and strain energy model. In some cases, relatively similar values of τ are observed for the same material across different models, suggesting a certain stability of the adjusted time-dependent response. In other cases, however, substantially different values are found, including considerably high values, such as in the Hartmann-Neff 7 terms adjustments for PA, PET, and HE PET, which differ markedly from the τ values obtained by other models for these same materials. Conversely, significantly lower values of τ are also observed in comparison with other formulations for same material, as in the Amin model adjustment for aramid, or in the Stumpf-Marczak and Veronda-Westmann models for the PA fiber. This behavior reinforces that the constant τ does not act in isolation, but rather in coupling with the functional form of W, so that its interpretation depends directly on the mathematical structure of the associated hyperelastic model and the tensor implementation.

Another noteworthy aspect is the recurrence of constants C_n with very low values, frequently close to the lower bounds imposed during the optimization process. At first glance, this behavior could suggest that certain terms of the strain energy function have negligible contribution. However, since the models employed are phenomenological and there is strong coupling among parameters within the fitting process, it is not appropriate to conclude, based solely on the numerical magnitude of the constants, that certain terms may be removed or simplified without affecting the constitutive response. Such an inference would require a specific investigation through a parametric sensitivity study capable of quantifying the real influence of each constant on the shape of the simulated curve and on the mean simulation error.

In this sense, a natural continuation of the present work consists of carrying out a parametric sensitivity study applied to the models with the best global performance. Based on the mean error analysis, the Stumpf-Marczak, Davies-De-Thomas, Modified Yeoh, and Bechir-Boufala-Chevalier models emerge as the most relevant candidates for this further investigation. A study of this nature may contribute to identifying the relative influence of each constant, verifying possible parametric redundancies, and discussing, with greater robustness, the admissible degree of simplification of each strain energy function for the different synthetic fibers analyzed.

In addition to fitting quality, parametric and computational complexity should also be considered in the assessment of constitutive models. Although processing times were not systematically recorded in the present study, experience during the execution of the simulations indicates that the computational effort tends to increase with the number of adjustable constants and with the mathematical complexity of the strain energy function. Models with fewer parameters, such as Neo-Hooke, Gent-Thomas, Humphrey-Yin, and Mooney-Rivlin 2 terms, achieved convergence in relatively short times, on the order of a few minutes, whereas more complex formulations, such as Hartmann-Neff 7 terms and Stumpf-Marczak, required longer optimization times, on the order of tens of minutes. The results also demonstrate that increasing the number of adjustable parameters does not systematically lead to lower fitting errors. Therefore, the choice of model should not be based solely on the lowest mean error, but also on the balance between accuracy, numerical robustness, and computational cost. Future studies may systematically quantify this cost by evaluating its relationship with the number of parameters, the dependence on the invariants I_1 and I_2, as well as the mathematical terms present in the strain energy function.

4. Conclusion

The present work proposed and evaluated a comprehensive approach for simulating the mechanical hysteresis behavior of synthetic fibers used in offshore mooring applications, combining a tensorial formulation based on continuum mechanics with different hyperelastic models defined by strain energy functions. The methodology incorporated finite deformations, the incompressibility assumption, viscoelastic memory through an internal variable, and parametric calibration by numerical optimization, using stabilized experimental curves obtained from cyclic dynamic tests as reference.

The main contribution of the study lies in the systematic evaluation of 140 material–model combinations under a unified experimental, constitutive, and computational framework. Rather than proposing a new strain energy function, the study investigates how twenty phenomenological hyperelastic formulations with different mathematical structures and parametric complexities perform when coupled with the same tensorial viscoelastic description and applied to seven synthetic fiber classes. This approach provides an exploratory comparative baseline for examining material-dependent and model-dependent trends in the simulation of stabilized mechanical hysteresis.

The comparison among the models showed that there is no single strain energy function universally superior for all analyzed fibers. Nevertheless, some models exhibited outstanding global performance, particularly Stumpf-Marczak ($\epsilon = 2.046\%$), Davies-De-Thomas ($\epsilon = 2.439\%$), Yeoh Modified ($\epsilon = 2.480\%$), and Bechir-Boufala-Chevalier ($\epsilon = 2.726\%$), which combined low mean errors with good constitutive representation capability across different materials. However, because the evaluated formulations differ in mathematical structure and number of adjustable parameters, these results should be interpreted as relative fitting performances rather than as an absolute ranking of models. On the other hand, it was also verified that simpler models may provide satisfactory performance with lower computational costs, an aspect of relevance for engineering applications and routine analyses.

In the comparison of the global performance of the numerical simulations with respect to the materials, lower mean errors were observed for aramid fibers ($\epsilon = 1.407\%$) and LCP fibers ($\epsilon = 2.110\%$), which exhibit a more linear behavior and greater similarity between the loading and unloading branches of the hysteresis cycle. In contrast, the highest mean error among the materials was found for polyamide ($\epsilon = 7.183\%$), whose mechanical hysteresis response presents successive changes in slope along the stress–strain curve.

The results reinforce that the selection of a constitutive model should simultaneously consider fitting accuracy, numerical robustness, parametric interpretability, and computational effort. In this way, the study establishes a consistent comparative basis for future applications involving synthetic fibers and offshore mooring systems. As a natural continuation of this research, future studies should focus on the parametric sensitivity of the most promising models, the comparative assessment of local and global optimization strategies (currently under development), the systematic quantification of the computational cost of each formulation, and the expansion of the methodology to other loading regimes and load amplitudes, different structural scales (rope yarns, strands, and sub-ropes), and materials with anisotropic behavior or more complex constitutive dependencies.

Author Contributions

D.M. da Cruz conceived the study, planned the experimental and numerical methodology, conducted the mechanical tests, processed and analyzed the experimental data, developed and implemented the numerical code, performed the constitutive simulations, analyzed the numerical results, prepared the figures and tables, and led the manuscript writing and journal correspondence. F.T. Stumpf contributed to the development and improvement of the numerical methodology, assisted in the interpretation of the constitutive modeling results, and contributed to the technical review of the manuscript. J.M. Vassoler contributed to the research supervision, contextualization of the engineering application, improvement of the numerical code, critical revision of the manuscript, and improvements in the presentation and scientific discussion of the work. The manuscript was written through the contribution of all authors. All authors discussed the results, reviewed, and approved the final version of the manuscript.

Acknowledgments

This study was financed in part by the Coordenação de Aperfeiçoamento de Pessoal de Nível Superior – Brazil (CAPES) – Finance Code 001, besides Conselho Nacional de Desenvolvimento Científico e Tecnológico (CNPq), Grant Number 140159/2026-6. We would also like to thank Fundação de Amparo à Pesquisa do Estado do Rio Grande do Sul (FAPERGS) and Financiadora de Estudos e Projetos (Finep) for its support. We would also like to thank the Policab Stress Analysis Laboratory for carrying out the mechanical tests.

Conflict of Interest

The authors declared no potential conflicts of interest concerning the research, authorship, and publication of this article.

Funding

The authors received no financial support for the research, authorship, and publication of this article.

Data Availability Statements

The datasets generated and/or analyzed during the current study are available from the corresponding author on reasonable request.

References

[1] Del Vecchio, C.J.M., *Light weight materials for deep water moorings*, Ph.D. Thesis, University of Reading, Reading, UK, 1992.
[2] Weller, S.D., Johanning, L., Davies, P., Banfield, S.J., Synthetic mooring ropes for marine renewable energy applications, *Renewable Energy*, 83, 2015, 1268-1278.
[3] Bastos, M.B., Silva, A.L.N., Evaluating Offshore Rope Fibers: Impact on Mooring Systems Integrity and Performance, *Offshore Technology Conference*, Houston, USA, OTC-30830-MS, 2020.
[4] Li, D., Lian, Y., Zheng, J., Chen, W., Liu, H., Yim, S.C., Review of Synthetic Fiber Ropes for Deepwater Moorings, *44th International Conference on Ocean, Offshore and Arctic Engineering*, Vancouver, Canada, 2025.
[5] McKenna, H.A., Hearle, J.W.S., O'Hear, N., *Handbook of fibre rope technology*, Woodhead Publishing, 2004.
[6] da Cruz, D.M., Zangalli, L.B., Barreto, M.A., da Silva, A.L.N., Bastos, I.N., Offshore mooring challenges for FOWT systems and MRE devices: Synthetic fiber solutions for mooring ropes, *Proceedings of the Rio Oil and Gas*, Rio de Janeiro, Brazil, 2024.
[7] Weller, S.D., Davies, P., Vickers, A.W., Johanning, L., Synthetic rope responses in the context of load history: Operational performance, *Ocean Engineering*, 83, 2014, 111-124.
[8] Lian, Y., Zhang, Y., Xie, Y., Zheng, J., Chen, W.X., Chen, S.C., Zhang, J., Xue, M.A., Yim, S.C., Effects of bedding-in loading history on mechanical behaviors of aramid HMPE and polyester mooring ropes, *Ocean Engineering*, 321, 2025, 120413.
[9] Lechat, C., Bunsell, A.R., Davies, P., Piant, A., Mechanical behaviour of polyethylene terephthalate & polyethylene naphthalate fibres under cyclic loading, *Journal of Materials Science*, 41(6), 2006, 1745-1756.
[10] Liu, H., Huang, W., Lian, Y., Li, L., An experimental investigation on nonlinear behaviors of synthetic fiber ropes for deepwater moorings under cyclic loading, *Applied Ocean Research*, 45, 2014, 22-32.
[11] Li, G., Li, W., Lin, S., Li, H., Ge, Y., Sun, Y., Dynamic stiffness of braided HMPE ropes under long-term cyclic loads: A full-scale experimental investigation, *Ocean Engineering*, 230, 2021, 109076.
[12] da Cruz, D.M., Begnini, G.R., Cruz Junior, A.J., Stumpf, F.T., Vassoler, J.M., Clain, F.M., Guilherme, C.E.M., Normalized stiffness assessment in mechanical protocol: polyester sub-ropes for offshore mooring systems, *Ships and Offshore Structures*, 2025, 1-17.
[13] Brinson, H.F., Brinson, L.C., *Polymer Engineering Science and Viscoelasticity: An Introduction*, Springer-Verlag New York, 2008.
[14] Khan, A.S., Lopez-Pamies, O., Kazmi, R., Thermo-mechanical large deformation response and constitutive modeling of viscoelastic polymers over a wide range of strain rates and temperatures, *International Journal of Plasticity*, 22(4), 2006, 581-601.
[15] Al-Rub, R.K.A., Tehrani, A.H., Darabi, M.K., Application of a large deformation nonlinear-viscoelastic viscoplastic viscodamage constitutive model to polymers and their composites, *International Journal of Damage Mechanics*, 24(2), 2015, 198-244.
[16] Fallahi, H., Taheri-Behrooz, F., Phenomenological constitutive modeling of the non-linear loading-unloading response of UD fiber-reinforced polymers, *Composite Structures*, 292, 2022, 115671.
[17] Nguyen, N., Thiagarajan, K., Nonlinear viscoelastic modeling of synthetic mooring lines, *Marine Structures*, 85, 2022, 103257.
[18] Talebi, S., Darijani, H., A pseudo-strain energy density function for mechanical behavior modeling of visco-hyperelastic materials, *International Journal of Mechanical Sciences*, 208, 2021, 106652.
[19] Portillo, F.J.S., Sempere, O.C., Marques, E.A.S., Lozano, M.S., Da Silva, L.F.M., Mechanical Characterisation and Comparison of Hyperelastic Adhesives: Modelling and Experimental Validation, *Journal of Applied and Computational Mechanics*, 8(1), 2022, 359-369.
[20] Shah, N.H., Ali, S.F., A hyperelastic strain energy function for isotropic rubberlike materials, *International Journal of Mechanical Sciences*, 279, 2024, 109472.
[21] Anssari-Benam, A., Hyperinelasticity: An energy-based constitutive modelling approach to isothermal large inelastic deformation of polymers. Part I, *Journal of the Mechanics and Physics of Solids*, 192, 2024, 105790.
[22] Eisenträger, S., Maurer, L., Juhre, D., Altenbach, H., Eisentraeger, J., Implementation of isotropic hyperelastic material models: a »template« approach, *Acta Mechanica*, 236(3), 2025, 1899-1934.
[23] Bahreman, M., Darijani, H., Fooladi, M., Constitutive modeling of isotropic hyperelastic materials using proposed phenomenological models in terms of strain invariants, *Polymer Engineering & Science*, 56(3), 2016, 299-308.
[24] Melly, S.K., Liu, L., Liu, Y., Leng, J., A review on material models for isotropic hyperelasticity, *International Journal of Mechanical System Dynamics*, 1(1), 2021, 71-88.
[25] Larbi, S., Tewfik, G., Mechri, A., Rezak, A., Optimization of a Specialized Forming Code for Rubber Products, *Journal of Applied and Computational Mechanics*, 2026, DOI: 10.22055/jacm.2026.48588.5345.
[26] da Cruz, D.M., Penaquioni, A., Zangalli, L.B., Bastos, M.B., Bastos, I.N., da Silva, A.L.N., Non-destructive testing of high-tenacity polyester sub-ropes for mooring systems, *Applied Ocean Research*, 134, 2023, 103513.
[27] Hoss, L., *Modelos constitutivos hiperelásticos para elastômeros incompressíveis: ajuste, comparação de desempenho e proposta de um novo modelo*, M.Sc. Thesis, Graduate Program in Mechanical Engineering, Federal University of Rio Grande do Sul, Porto Alegre, Brazil, 2009.
[28] da Cruz, D.M., *Estudo teórico, experimental e numérico do comportamento viscoelástico e caracterização de fibras sintéticas poliméricas*, B.Sc. Thesis, School of Engineering, Federal University of Rio Grande, Rio Grande, Brazil, 2022.

[29] Stumpf, F.T., Guilherme, C.E.M., da Cruz, D.M., da Silva, A.H.M.F.T., Bastos, M.B., A general constitutive model for the numerical simulation of different synthetic fibres used in offshore mooring, *Ships and Offshore Structures*, 18(9), 2023, 1338-1344.
[30] da Cruz, D.M., Guilherme, C.E.M., Stumpf, F.T., Bastos, M.B., Numerical Assessment of Mechanical Behavior of Mooring Lines Using Hybrid Synthetic Fiber-Rope Segments, *Offshore Technology Conference*, Houston, USA, OTC-31906-MS, 2022.
[31] Stumpf, F.T., Barreto, M.A., da Cruz, D.M., Guilherme, C.E.M., Numerical simulation of multi-material hybrid lines for offshore mooring, *Ocean Engineering*, 305, 2024, 117979.
[32] da Cruz, D.M., Popiolek Júnior, T.L., Barreto, M.A., Guilherme, C.E.M., Stumpf, F.T., Evaluation of energy models for numerical simulation of the mechanical behavior of polyester multifilaments, *The Journal of Engineering and Exact Sciences*, 9(1), 2023, 15321–01e.
[33] da Cruz, D.M., Barreto, M.A., Zangalli, L.B., Stumpf, F.T., Vassoler, J.M., Guilherme, C.E.M., Numerical simulation of the stress-strain behavior of polymeric fibers for mooring offshore structures, *Proceedings XLIV Ibero-Latin American Congress on Computational Methods in Engineering*, Porto, Portugal, 2023.
[34] da Cruz, D.M., Popiolek Júnior, T.L., Barreto, M.A., de Souza, S.P., Zangalli, L.B., Cruz Junior, A.J., Martins, T.C., da Silva, A.L.N., Bastos, I.N., Guilherme, C.E.M., Numerical simulation with hyperelastic constitutive model for high-performance multifilaments used in offshore mooring ropes, *The Journal of Engineering and Exact Sciences*, 10(2), 2024, 17255.
[35] da Cruz, D.M., Zangalli, L.B., Barreto, M.A., da Silva, A.L.N., Bastos, I.N., Numerical Simulation of Creep Behavior in Low Creep HMPE Fibers Used for Offshore Mooring Ropes, *Offshore Technology Conference Brasil*, Rio de Janeiro, Brazil, OTC-36033-MS, 2025.
[36] da Cruz, D.M., Bastos, I.N., da Silva, A.L.N., Vassoler, J.M., Stumpf, F.T., Cruz Junior, A.J., Martins, T.C., Clain, F.M., Guilherme, C.E.M., Dynamic Cycle Simulation in Offshore Mooring Fibers: Modified Mathematical Models and Dependence on Invariants of Continuum Mechanics, *VETOR - Journal of Exact Sciences and Engineering*, 35(1), 2025, e18256.
[37] da Cruz, D.M., Zangalli, L.B., Barreto, M.A., Bastos, I.N., da Silva, A.L.N., Numerical simulation of the stress-strain behavior of polyester subropes for offshore mooring and relationship with change stiffness during the test protocol, *Proceedings of the Rio Oil and Gas*, Rio de Janeiro, Brazil, 2024.
[38] da Cruz, D.M., Zangalli, L.B., Cruz Junior, A.J., da Silva, A.L.N., Bastos, I.N., Guilherme, C.E.M., Clain, F.M., Vassoler, J.M., Stumpf, F.T., Constitutive Simulation of Synthetic Fibers for Offshore Mooring Under Cyclic Loading: Hysteresis Stabilization and Stiffness Evolution, *Proceedings XLVI Ibero-Latin American Congress on Computational Methods in Engineering*, Vitória, Brazil, 2025.
[39] da Cruz, D.M., Popiolek Júnior, T.L., Bastos, I.N., da Silva, A.P., da Silva, A.L.N., Vassoler, J.M., Stumpf, F.T., Numerical Modeling of the Stress-Strain Response in Progressive Loading Cycles of Polyester Multifilaments, *Anais do XXVIII Encontro Nacional de Modelagem Computacional e XVI Encontro de Ciência e Tecnologia de Materiais*, Montes Claros, Brazil, 2025.
[40] American Society for Testing and Materials, *Standard Test Methods for Linear Density of Textile Fibers*, ASTM D1577-07, 2018.
[41] International Organization for Standardization, *Textiles — Yarns from packages — Determination of single-end breaking force and elongation at break using constant rate of extension (CRE) tester*, ISO 2062, 2009.
[42] International Organization for Standardization, *Textiles — Standard atmospheres for conditioning and testing*, ISO 139, 2005.
[43] Simo, J.C., Hughes, T.J.R., *Computational Inelasticity*, Springer Science & Business Media, 2006.
[44] Flory, P.J., Thermodynamic relations for high elastic materials, *Transactions of the Faraday Society*, 57, 1961, 829-838.
[45] The MathWorks, Inc., fmincon: Solve constrained nonlinear multivariable minimization problem, 2026, https://www.mathworks.com/help/optim/ug/fmincon.html.
[46] Holzapfel, G.A., *Nonlinear Solid Mechanics: A Continuum Approach for Engineering Science*, John Wiley & Sons, 2000.
[47] Truesdell, C., Noll, W., *The Non-Linear Field Theories of Mechanics*, Springer-Verlag Berlin, 1965.
[48] Beatty, M.F., Topics in Finite Elasticity: Hyperelasticity of Rubber, Elastomers, and Biological Tissues—With Examples, *Applied Mechanics Reviews*, 40(12), 1987, 1699-1734.
[49] Amin, A.F.M.S., Alam, M.S., Okui, Y., An improved hyperelasticity relation in modeling viscoelasticity response of natural and high damping rubbers in compression: experiments, parameter identification and numerical verification, *Mechanics of Materials*, 34(2), 2002, 75-95.
[50] Bechir, H., Boufala, K., Chevalier, Y., Strain energy density function for carbon black filled rubber vulcanized for industrial applications, *Mécanique & Industries*, 3(3), 2002, 245-252.
[51] Davies, C.K.L., De, D.K., Thomas, A.G., Characterization of the Behavior of Rubber for Engineering Design Purposes. 1. Stress-Strain Relations, *Rubber Chemistry and Technology*, 67(4), 1994, 716-728.
[52] Gent, A.N., Thomas, A.G., Forms for the stored (strain) energy function for vulcanized rubber, *Journal of Polymer Science*, 28(118), 1958, 625-628.
[53] Hartmann, S., Neff, P., Polyconvexity of generalized polynomial-type hyperelastic strain energy functions for near-incompressibility, *International Journal of Solids and Structures*, 40 (11), 2003, 2767-2791.
[54] Humphrey, J.D., Yin, F.C.P., On Constitutive Relations and Finite Deformations of Passive Cardiac Tissue: I. A Pseudostrain-Energy Function, *Journal of Biomechanical Engineering*, 109(4), 1987, 298-304.
[55] Knowles, J.K., The finite anti-plane shear field near the tip of a crack for a class of incompressible elastic solids, *International Journal of Fracture*, 13(5), 1977, 611-639.
[56] Mooney, M., A Theory of Large Elastic Deformation, *Journal of Applied Physics*, 11(9), 1940, 582-592.
[57] Rivlin, R.S., Saunders, D.W., Large elastic deformations of isotropic materials VII. Experiments on the deformation of rubber, *Philosophical Transactions of the Royal Society of London, Series A: Mathematical and Physical Sciences*, 243(865), 1951, 251-288.
[58] Treloar, L.R.G., The elasticity and related properties of rubbers, *Reports on Progress in Physics*, 36(7), 1973, 755-826.
[59] Stumpf, F.T., Marczak, R.J., Constitutive framework of a new hyperelastic model for isotropic rubber-like materials for finite element implementation, *Latin American Journal of Solids and Structures*, 18(2), 2021, e346.
[60] Veronda, D.R., Westmann, R.A., Mechanical characterization of skin—Finite deformations, *Journal of Biomechanics*, 3(1), 1970, 111-124.
[61] Yamashita, Y., Kawabata, S., Approximated form of the strain energy-density function of carbon black filled rubbers for industrial applications, *International Polymer Science and Technology*, 20, 1993, T-52.
[62] Yeoh, O.H., Characterization of Elastic Properties of Carbon-Black-Filled Rubber Vulcanizates, *Rubber Chemistry and Technology*, 63(5), 1990, 792-805.
[63] Yeoh, O.H., Some Forms of the Strain Energy Function for Rubber, *Rubber Chemistry and Technology*, 66(5), 1993, 754-771.
[64] Seyfi, B., Rassoli, A., Imeni Markhali, M., Fatouraee, N., Characterization of the Nonlinear Biaxial Mechanical Behavior of Human Ureter using Constitutive Modeling and Artificial Neural Networks, *Journal of Applied and Computational Mechanics*, 8(4), 2022, 1186-1195.
[65] Topol, H., Al-Chlaihawi, M.J., Demirkoparan, H., Merodio, J., Bifurcation of Fiber-Reinforced Cylindrical Membranes under Extension, Inflation, and Swelling, *Journal of Applied and Computational Mechanics*, 9(1), 2023, 113-128.
[66] Al-Chlaihawi, M.J., Font, A., Topol, H., Demirkoparan, H., Merodio, J., Bulging and Bending of a Thick-Walled Cylinder with Residual Stress under Combined Extension and Inflation, *Journal of Applied and Computational Mechanics*, 12(3), 2026, 1256-1275.
[67] Asth, L.S., de Lima, K.C., Moreira, C.S., Knupp, D.C., Stutz, L.T., Parameter Estimation and Strain Energy Model Class Selection for a Hyperelastic Composite Under Compression, *VETOR - Journal of Exact Sciences and Engineering*, 36(1), 2026, e20864.

Appendix A

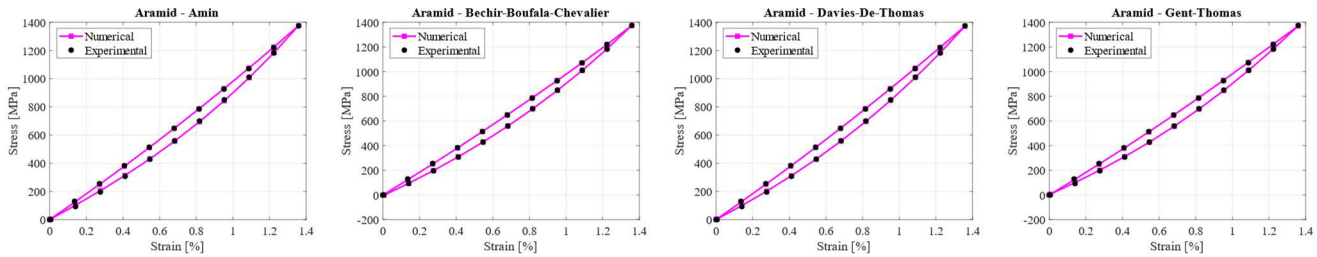

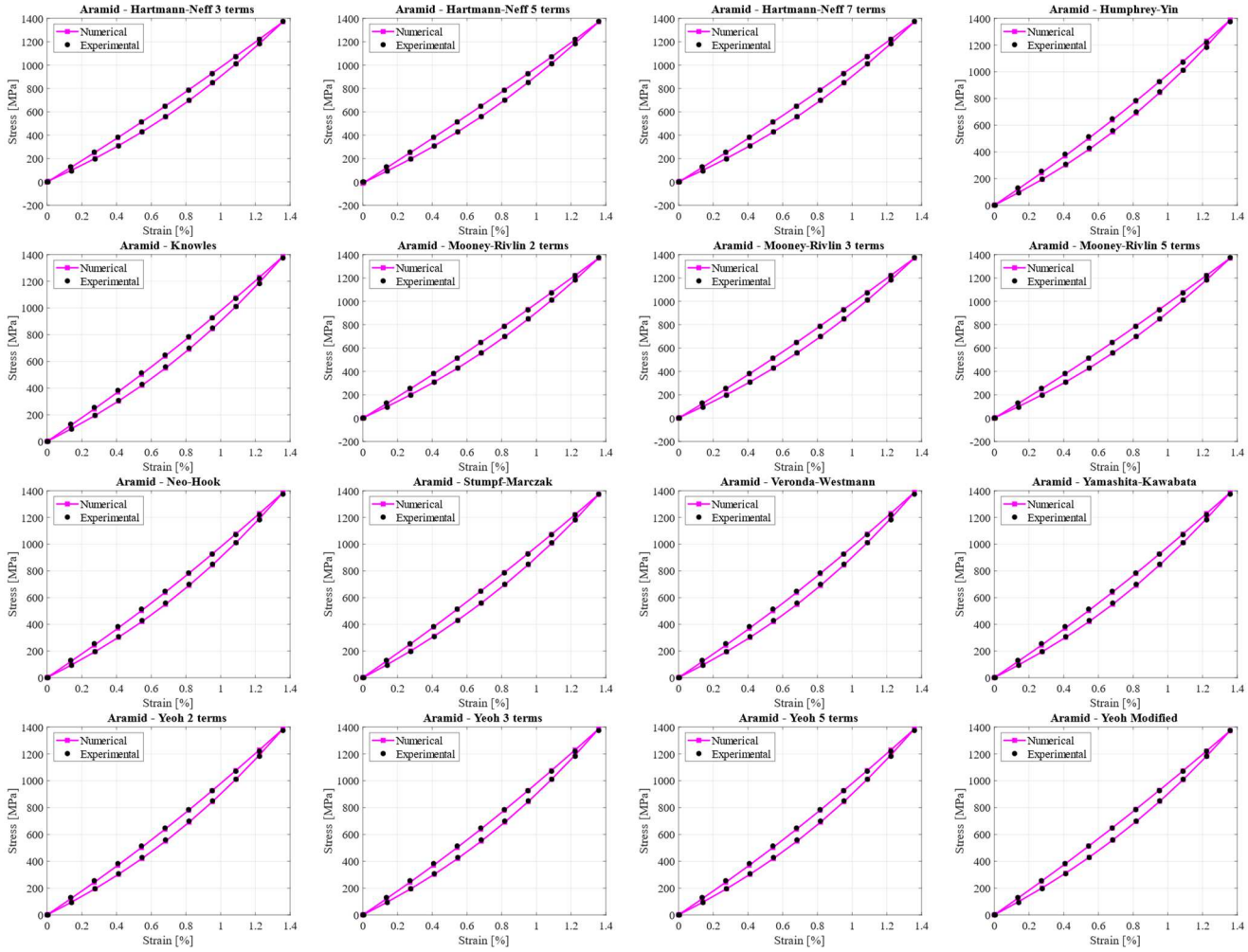
Aramid - Hartmann-Neff 3 terms
Aramid - Hartmann-Neff 5 terms
Aramid - Hartmann-Neff 7 terms
Aramid - Humphrey-Yin
Aramid - Knowles
Aramid - Mooney-Rivlin 2 terms
Aramid - Mooney-Rivlin 3 terms
Aramid - Mooney-Rivlin 5 terms
Aramid - Neo-Hook
Aramid - Stumpf-Marczak
Aramid - Veronda-Westmann
Aramid - Yamashita-Kawabata
Aramid - Yeoh 2 terms
Aramid - Yeoh 3 terms
Aramid - Yeoh 5 terms
Aramid - Yeoh Modified
Numerical
Experimental
Stress [MPa]
Strain [%]

Appendix B

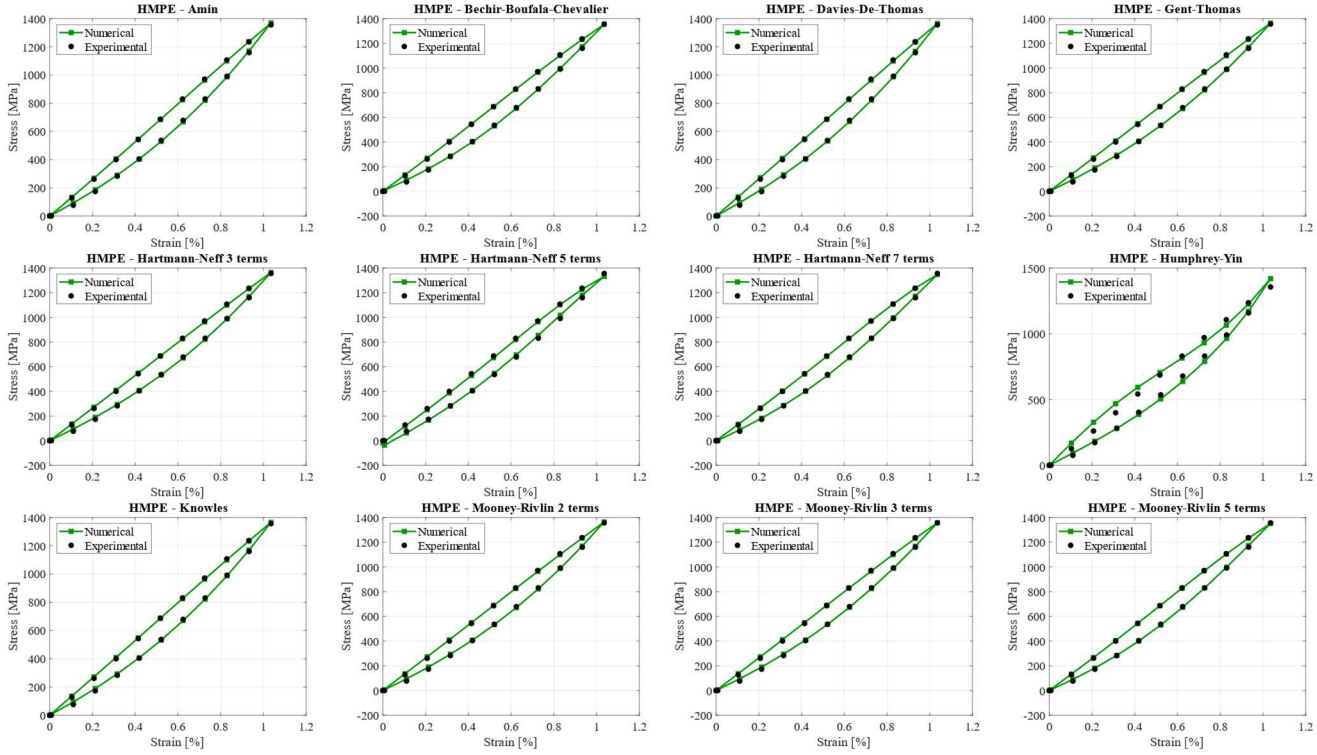
HMPE - Amin
HMPE - Bechir-Boufala-Chevalier
HMPE - Davies-De-Thomas
HMPE - Gent-Thomas
HMPE - Hartmann-Neff 3 terms
HMPE - Hartmann-Neff 5 terms
HMPE - Hartmann-Neff 7 terms
HMPE - Humphrey-Yin
HMPE - Knowles
HMPE - Mooney-Rivlin 2 terms
HMPE - Mooney-Rivlin 3 terms
HMPE - Mooney-Rivlin 5 terms
Numerical
Experimental
Stress [MPa]
Strain [%]

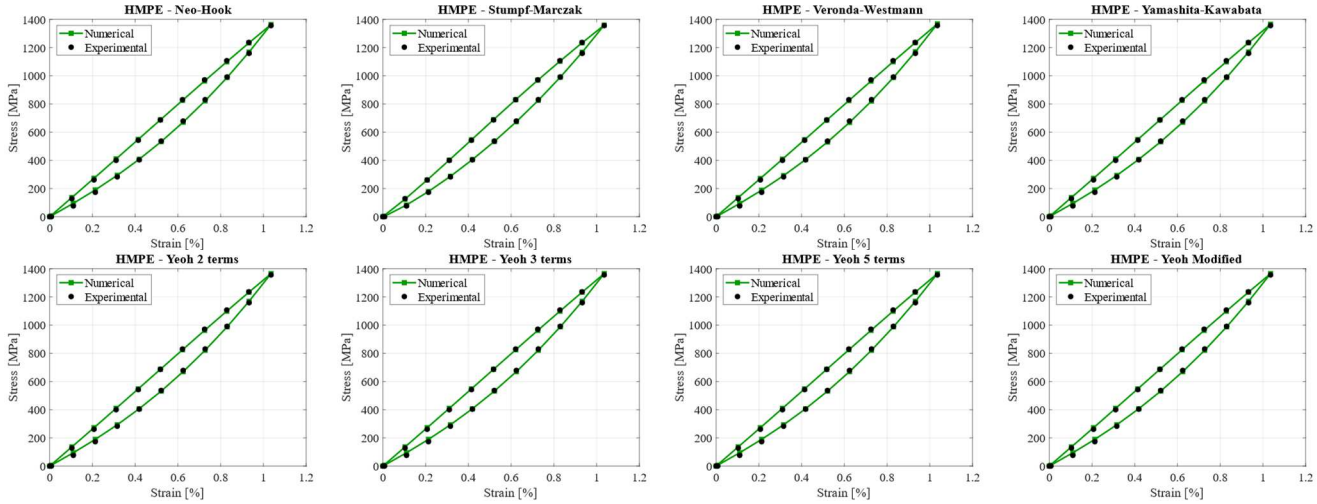
HMPE - Neo-Hook
HMPE - Stumpf-Marczak
HMPE - Veronda-Westmann
HMPE - Yamashita-Kawabata
HMPE - Yeoh 2 terms
HMPE - Yeoh 3 terms
HMPE - Yeoh 5 terms
HMPE - Yeoh Modified
Numerical
Experimental
Stress [MPa]
Strain [%]

Appendix C

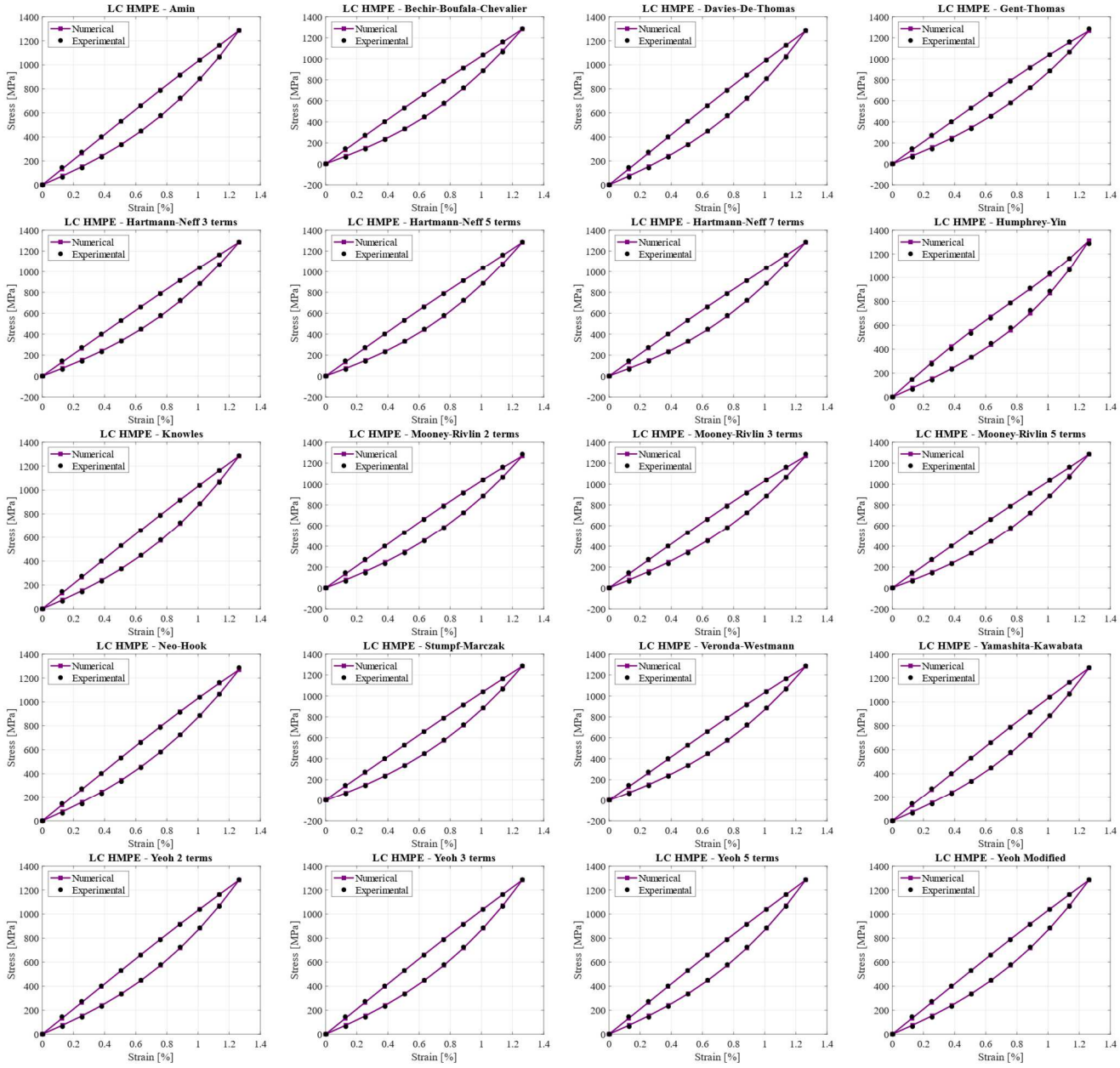
LC HMPE - Amin
LC HMPE - Bechir-Boufala-Chevalier
LC HMPE - Davies-De-Thomas
LC HMPE - Gent-Thomas
LC HMPE - Hartmann-Neff 3 terms
LC HMPE - Hartmann-Neff 5 terms
LC HMPE - Hartmann-Neff 7 terms
LC HMPE - Humphrey-Yin
LC HMPE - Knowles
LC HMPE - Mooney-Rivlin 2 terms
LC HMPE - Mooney-Rivlin 3 terms
LC HMPE - Mooney-Rivlin 5 terms
LC HMPE - Neo-Hook
LC HMPE - Stumpf-Marczak
LC HMPE - Veronda-Westmann
LC HMPE - Yamashita-Kawabata
LC HMPE - Yeoh 2 terms
LC HMPE - Yeoh 3 terms
LC HMPE - Yeoh 5 terms
LC HMPE - Yeoh Modified
Numerical
Experimental
Stress [MPa]
Strain [%]

Appendix D

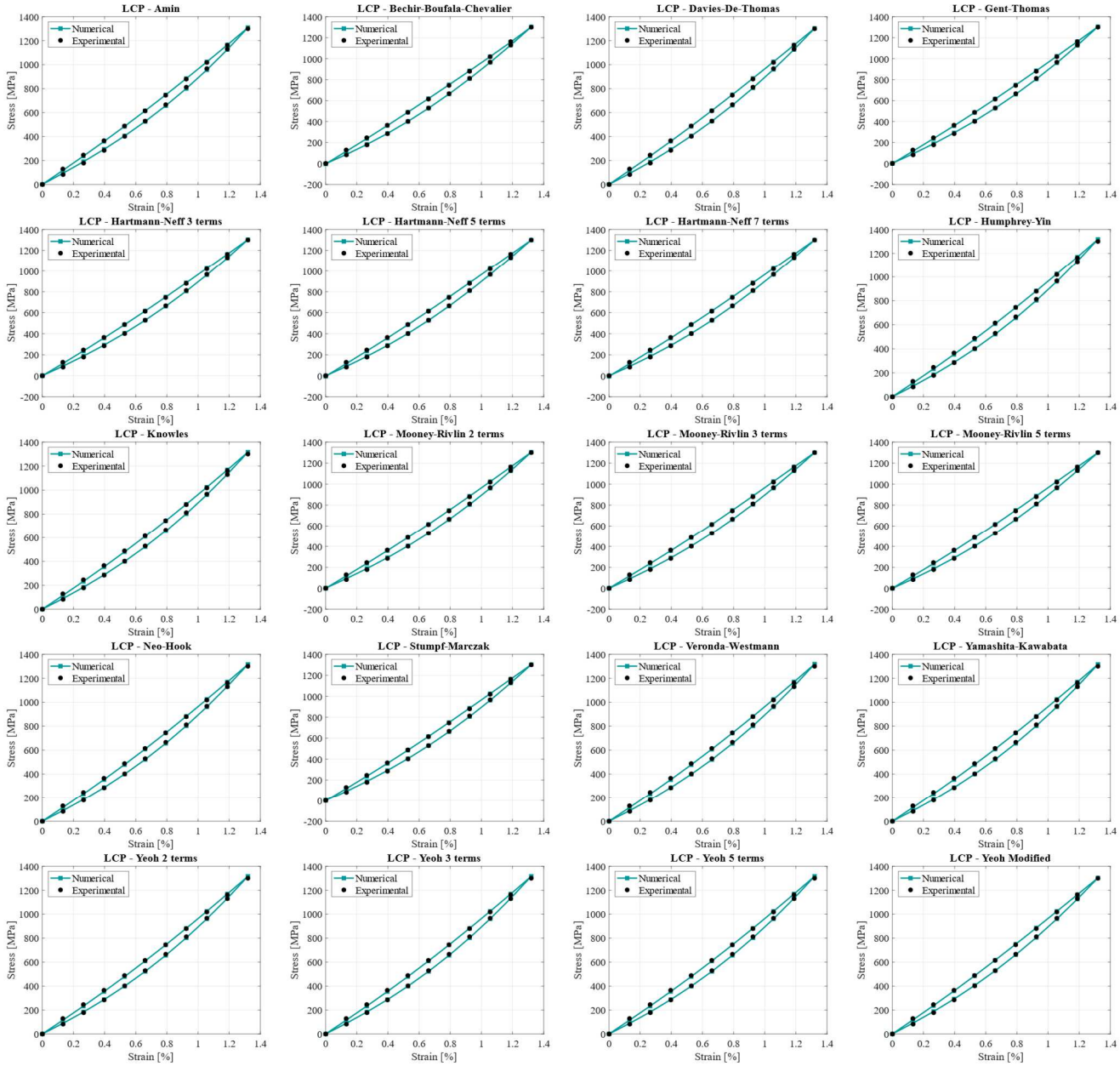

Appendix E

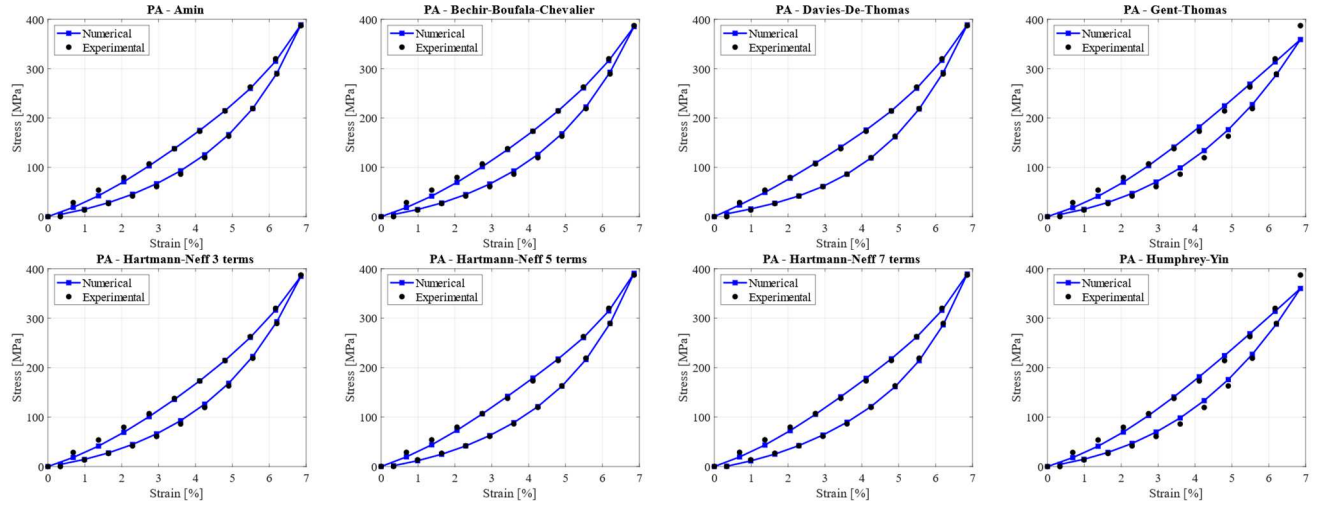

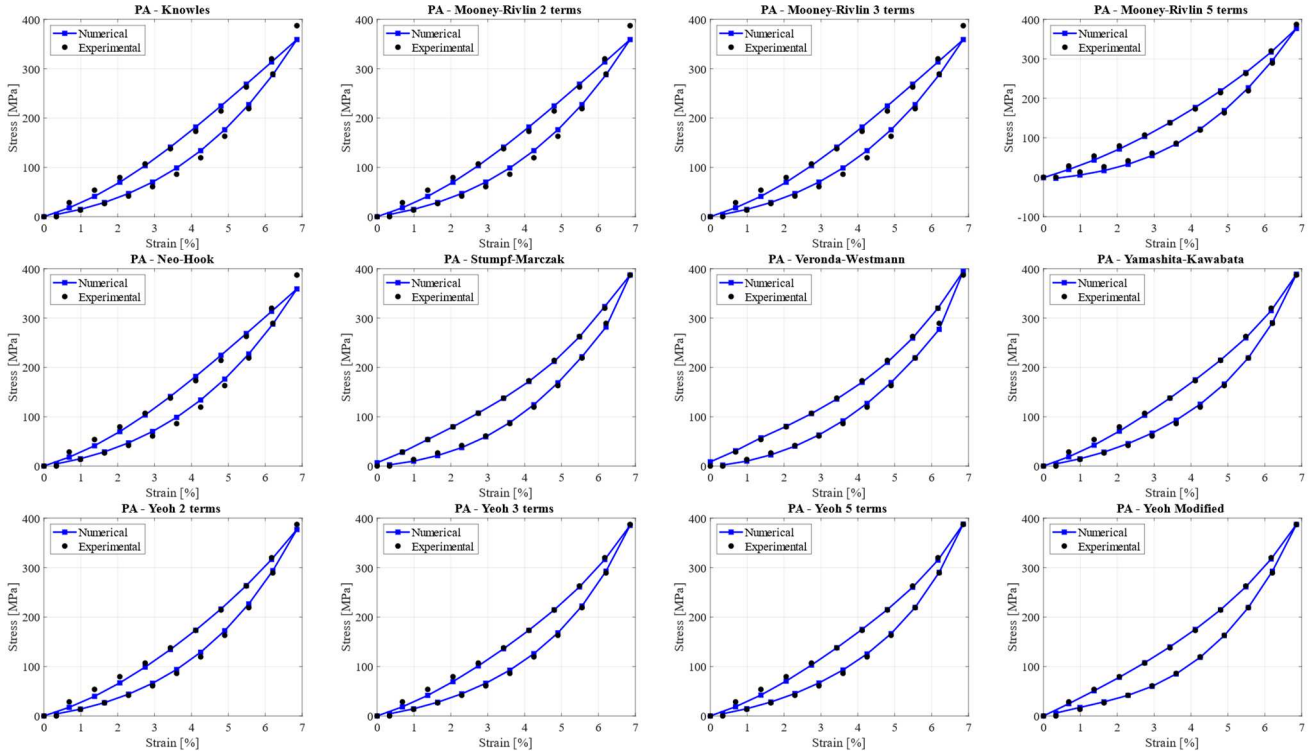
PA - Knowles
PA - Mooney-Rivlin 2 terms
PA - Mooney-Rivlin 3 terms
PA - Mooney-Rivlin 5 terms
PA - Neo-Hook
PA - Stumpf-Marczak
PA - Veronda-Westmann
PA - Yamashita-Kawabata
PA - Yeoh 2 terms
PA - Yeoh 3 terms
PA - Yeoh 5 terms
PA - Yeoh Modified
Numerical
Experimental
Stress [MPa]
Strain [%]

Appendix F

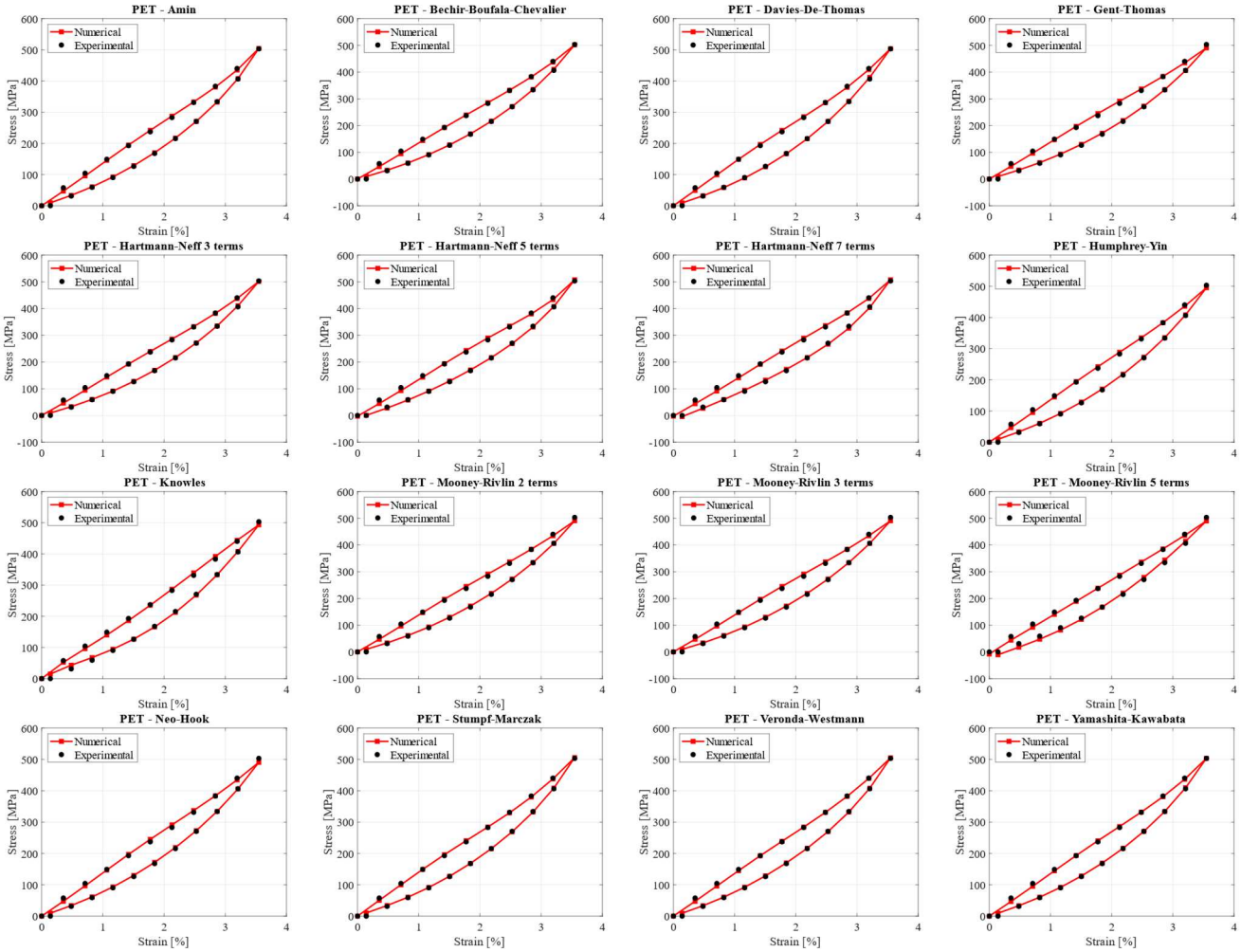
PET - Amin
PET - Bechir-Boufala-Chevalier
PET - Davies-De-Thomas
PET - Gent-Thomas
PET - Hartmann-Neff 3 terms
PET - Hartmann-Neff 5 terms
PET - Hartmann-Neff 7 terms
PET - Humphrey-Yin
PET - Knowles
PET - Mooney-Rivlin 2 terms
PET - Mooney-Rivlin 3 terms
PET - Mooney-Rivlin 5 terms
PET - Neo-Hook
PET - Stumpf-Marczak
PET - Veronda-Westmann
PET - Yamashita-Kawabata
Numerical
Experimental
Stress [MPa]
Strain [%]

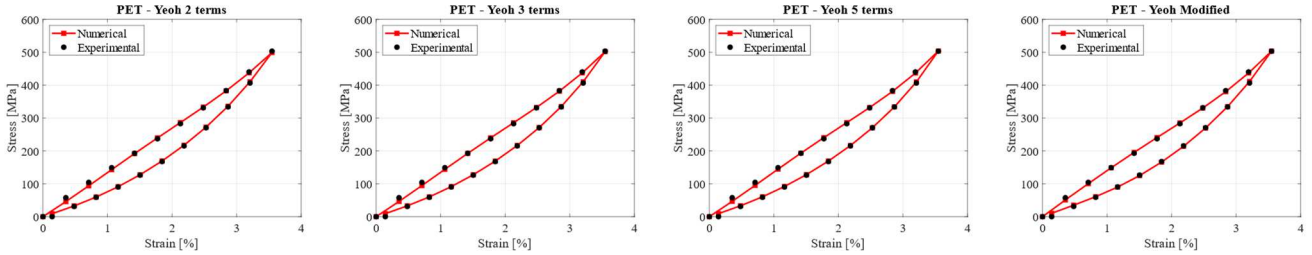

Appendix G

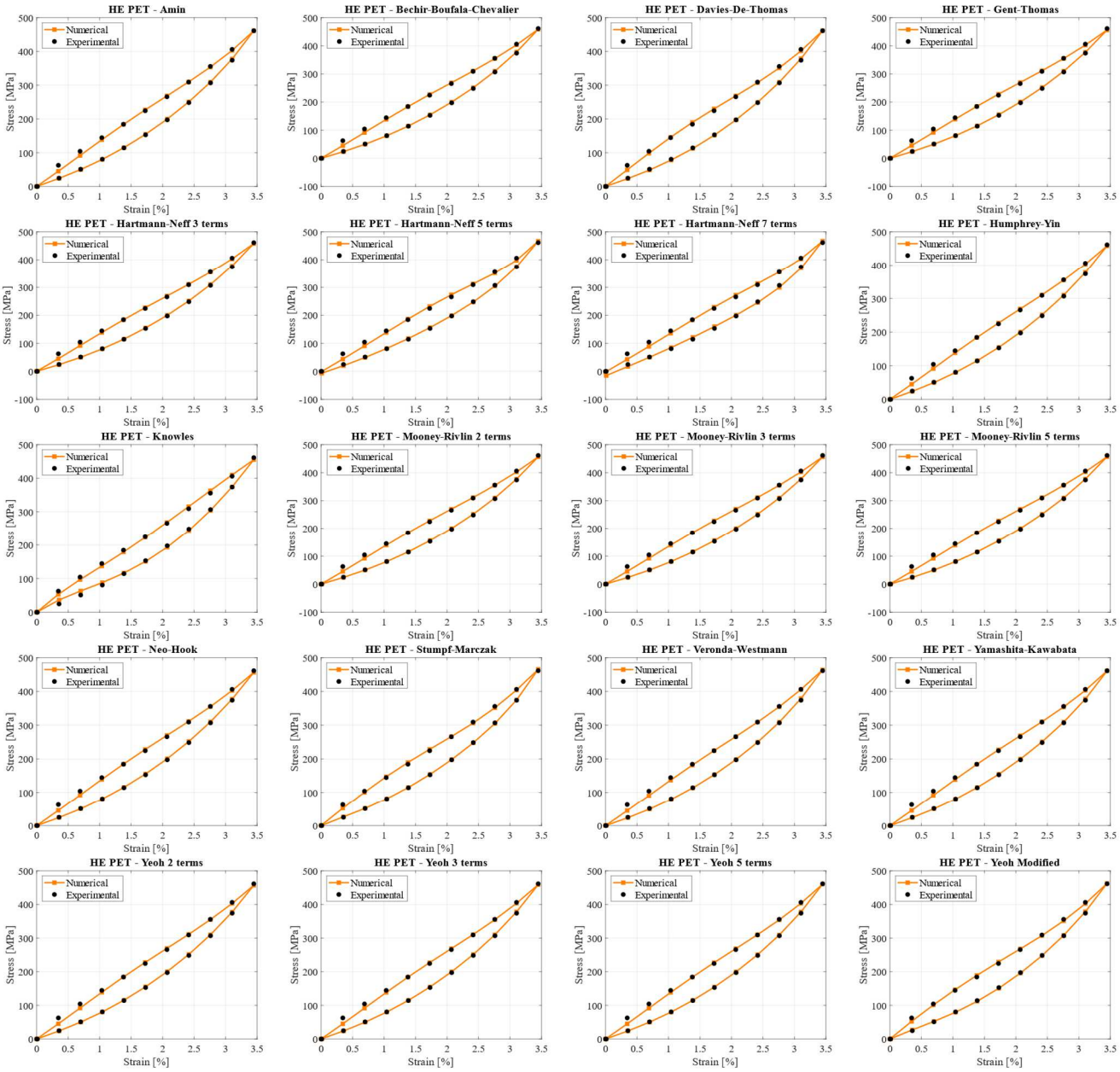

Appendix H

Table H1. Constants obtained in parametric optimization, all fibers, Amin model.

Constants	Aramid	HMPE	LC HMPE	LCP	PA	PET	HE PET
γ	0.655	0.500	0.500	0.500	0.510	0.500	0.501
τ	14.679	132.046	80.776	100.977	37.921	22.220	20.333
C_1	5.005	197.851	173.438	74.313	4.232	21.849	21.764
C_2	3.877	1.00×10^{-8}	3.90×10^{-7}	$< 1.00 \times 10^{-8}$	6.48×10^{-6}	1.70×10^{-7}	3.30×10^{-7}
C_3	5.485	43.519	5.434	146.991	2.10×10^{-7}	1.15×10^{-3}	1.90×10^{-6}
C_4	3.044	4.670	13.976	55.159	2.951	5.362	4.886
C_5	0.529	0.094	0.706	9.85×10^{-6}	0.485	0.355	0.117

Table H2. Constants obtained in parametric optimization, all fibers, Bechir-Boufala-Chevalier model.

Constants	Aramid	HMPE	LC HMPE	LCP	PA	PET	HE PET
γ	0.500	0.500	0.500	0.500	0.500	0.500	0.499
τ	367.271	130.594	53.680	300.530	36.157	22.120	20.398
C_1	150.988	214.362	177.325	142.335	4.162	21.607	21.746
C_2	2.815	3.30×10^{-7}	1.20×10^{-7}	12.232	$< 1.00 \times 10^{-8}$	$< 1.00 \times 10^{-8}$	8.00×10^{-8}
C_3	1.82×10^{-4}	12.878	7.893	10.824	$< 1.00 \times 10^{-8}$	$< 1.00 \times 10^{-8}$	4.00×10^{-8}
C_4	6.713	12.645	3.123	12.538	$< 1.00 \times 10^{-8}$	$< 1.00 \times 10^{-8}$	1.00×10^{-8}
C_5	1.508	1.90×10^{-7}	8.00×10^{-8}	2.004	1.13×10^{-4}	0.001	2.76×10^{-4}

Table H3. Constants obtained in parametric optimization, all fibers, Davies-De-Thomas model.

Constants	Aramid	HMPE	LC HMPE	LCP	PA	PET	HE PET
γ	0.499	0.500	0.500	0.500	0.500	0.500	0.500
τ	310.374	157.702	81.773	305.560	25.356	19.354	17.429
C_1	1046.838	436.686	489.057	1058.079	10.289	41.628	42.247
C_2	1.262	1.00×10^{-8}	0.288	0.824	0.345	0.010	0.011
C_3	2.660	0.765	3.249	4.702	0.689	1.00×10^{-8}	$< 1.00 \times 10^{-8}$
C_4	3.039	0.332	2.901	0.002	0.026	0.073	0.049

Table H4. Constants obtained in parametric optimization, all fibers, Gent-Thomas model.

Constants	Aramid	HMPE	LC HMPE	LCP	PA	PET	HE PET
γ	0.500	0.500	0.500	0.500	0.500	0.500	0.500
τ	289.317	158.445	90.409	292.220	67.137	22.638	20.385
C_1	149.696	218.747	175.462	146.841	4.044	22.033	21.864
C_2	3.412	4.00×10^{-8}	1.80×10^{-7}	2.612	3.00×10^{-8}	4.30×10^{-7}	2.00×10^{-8}

Table H5. Constants obtained in parametric optimization, all fibers, Hartmann-Neff 3terms model.

Constants	Aramid	HMPE	LC HMPE	LCP	PA	PET	HE PET
γ	0.500	0.500	0.500	0.500	0.500	0.500	0.499
τ	285.975	158.209	82.562	296.655	36.156	22.156	20.401
C_1	0.093	0.009	0.128	3.10×10^{-7}	1.04×10^{-4}	0.001	1.78×10^{-4}
C_2	146.898	218.380	170.980	146.981	4.139	21.525	21.748
C_3	1.594	1.50×10^{-7}	2.00×10^{-8}	0.670	$< 1.00 \times 10^{-8}$	3.80×10^{-7}	2.00×10^{-8}

Table H6. Constants obtained in parametric optimization, all fibers, Hartmann-Neff 5terms model.

Constants	Aramid	HMPE	LC HMPE	LCP	PA	PET	HE PET
γ	0.500	0.500	0.500	0.500	0.474	0.502	0.500
τ	423.894	592.634	52.162	308.182	420.499	415.079	306.151
C_1	1.993	6.340	1.46×10^{-6}	0.997	0.001	0.053	0.068
C_2	84.569	3.01×10^{-5}	177.455	114.526	4.424	19.585	19.265
C_3	4.89×10^{-5}	5.96×10^{-6}	8.286	4.70×10^{-6}	0.059	0.578	3.85×10^{-5}
C_4	11.133	20.184	4.40×10^{-7}	4.513	0.046	0.913	0.714
C_5	1.000	6.464	0.385	0.691	3.53×10^{-4}	0.016	0.024

Table H7. Constants obtained in parametric optimization, all fibers, Hartmann-Neff 7terms model.

Constants	Aramid	HMPE	LC HMPE	LCP	PA	PET	HE PET
γ	0.505	0.494	0.500	0.500	0.503	0.503	0.006
τ	285.573	177.280	52.162	308.182	7525.069	7525.088	1836.402
C_1	0.147	0.745	7.31×10^{-6}	0.997	0.001	0.024	0.029
C_2	145.170	192.300	177.455	114.526	4.410	19.946	20.065
C_3	3.48×10^{-6}	0.001	4.165	9.40×10^{-7}	0.034	0.279	0.257
C_4	3.48×10^{-6}	0.001	4.122	9.40×10^{-7}	0.033	0.279	0.257
C_5	1.817	5.20×10^{-6}	2.19×10^{-6}	4.513	0.051	0.834	0.909
C_6	0.034	0.351	0.385	0.691	$< 1.00 \times 10^{-8}$	$< 1.00 \times 10^{-8}$	4.00×10^{-8}
C_7	4.00×10^{-8}	0.306	7.00×10^{-8}	2.00×10^{-8}	1.00×10^{-8}	1.00×10^{-8}	7.00×10^{-7}

Table H8. Constants obtained in parametric optimization, all fibers, Humphrey-Yin model.

Constants	Aramid	HMPE	LC HMPE	LCP	PA	PET	HE PET
γ	0.500	0.500	0.500	0.500	0.500	0.500	0.500
τ	300.946	18.839	30.882	300.752	64.909	22.357	20.434
C_1	62858.634	2020.894	2354.142	62858.646	13517.734	13517.114	30690.456
C_2	0.002	0.138	0.082	0.002	2.99×10^{-4}	0.002	0.001

Table H9. Constants obtained in parametric optimization, all fibers, Knowles model.

Constants	Aramid	HMPE	LC HMPE	LCP	PA	PET	HE PET
γ	0.500	0.501	0.495	0.500	0.543	0.500	0.500
τ	301.196	157.715	81.615	301.025	67.137	193.171	205.260
C_1	294.127	436.700	348.123	289.952	8.089	53.924	55.035
C_2	$< 1.00 \times 10^{-8}$	0.003	0.021	$< 1.00 \times 10^{-8}$	$< 1.00 \times 10^{-8}$	0.859	0.052
C_3	114.880	115.739	115.760	113.731	0.982	0.452	0.066

Table H10. Constants obtained in parametric optimization, all fibers, Mooney-Rivlin 2 terms model.

Constants	Aramid	HMPE	LC HMPE	LCP	PA	PET	HE PET
γ	0.500	0.500	0.500	0.500	0.500	0.500	0.500
τ	293.381	158.445	90.409	294.989	67.137	22.638	20.385
C_1	149.738	218.747	175.462	146.960	4.044	22.033	21.864
C_2	2.495	1.35×10^{-6}	7.00×10^{-8}	2.005	2.00×10^{-8}	3.00×10^{-8}	3.00×10^{-8}

Table H11. Constants obtained in parametric optimization, all fibers, Mooney-Rivlin 3 terms model.

Constants	Aramid	HMPE	LC HMPE	LCP	PA	PET	HE PET
γ	0.500	0.500	0.500	0.500	0.732	0.500	0.500
τ	293.381	158.484	90.409	310.781	67.137	22.638	20.385
C_1	149.738	219.016	175.462	146.390	4.044	22.033	21.864
C_2	2.495	1.40×10^{-7}	$< 1.00 \times 10^{-8}$	0.457	$< 1.00 \times 10^{-8}$	1.00×10^{-8}	5.00×10^{-8}
C_3	3.90×10^{-7}	2.275	2.00×10^{-8}	1.218	1.00×10^{-8}	3.00×10^{-8}	2.00×10^{-8}

Table H12. Constants obtained in parametric optimization, all fibers, Mooney-Rivlin 5 terms model.

Constants	Aramid	HMPE	LC HMPE	LCP	PA	PET	HE PET
γ	0.500	0.500	0.500	0.500	0.500	0.500	0.500
τ	293.381	138.185	53.680	310.927	1329.223	1169.417	20.395
C_1	149.738	212.848	177.325	146.438	4.973	21.682	21.818
C_2	2.495	8.00×10^{-8}	4.90×10^{-7}	4.31×10^{-5}	0.518	7.224	$< 1.00 \times 10^{-8}$
C_3	1.83×10^{-6}	16.178	1.12×10^{-5}	4.62×10^{-6}	$< 1.00 \times 10^{-8}$	$< 1.00 \times 10^{-8}$	$< 1.00 \times 10^{-8}$
C_4	6.08×10^{-6}	6.954	7.893	0.663	0.270	3.587	0.002
C_5	4.14×10^{-6}	5.20×10^{-7}	3.123	1.428	2.00×10^{-8}	2.00×10^{-8}	2.00×10^{-8}

Table H13. Constants obtained in parametric optimization, all fibers, Neo-Hooke model.

Constants	Aramid	HMPE	LC HMPE	LCP	PA	PET	HE PET
γ	0.500	0.500	0.500	0.500	0.500	0.500	0.500
τ	301.196	158.445	90.409	301.025	67.137	22.638	20.385
C_1	147.064	218.747	175.462	144.976	4.044	22.033	21.864

Table H14. Constants obtained in parametric optimization, all fibers, Stumpf-Marczak model.

Constants	Aramid	HMPE	LC HMPE	LCP	PA	PET	HE PET
γ	0.500	0.500	0.500	0.503	0.500	0.500	0.500
τ	318.848	121.873	227.375	303.860	0.944	17.608	15.007
C_1	128.520	156.079	68.885	120.426	−7.753	21.386	21.854
C_2	0.237	0.283	0.392	0.048	0.006	−0.004	−0.001
C_3	3.552	962.547	−0.011	0.897	−0.017	0.003	−0.951
C_4	1.503	1.232	-2.70×10^{-5}	1.276	1.001	0.001	−0.362
C_5	47.206	59.038	438.689	53.501	25.148	6.222	9.335
C_6	−2.462	−2.097	−7.793	0.052	−2.996	−0.060	−0.093

Table H15. Constants obtained in parametric optimization, all fibers, Veronda-Westmann model.

Constants	Aramid	HMPE	LC HMPE	LCP	PA	PET	HE PET
γ	0.500	0.500	0.500	0.500	0.506	0.500	0.500
τ	300.883	157.652	88.743	300.617	1.104	17.933	19.094
C_1	43938.229	43934.456	43932.777	43938.252	943.399	13517.091	13517.098
C_2	8.98×10^{-5}	0.571	1.981	1.21×10^{-4}	3.814	0.154	0.056
C_3	0.003	0.005	0.004	0.003	0.005	0.002	0.002

Table H16. Constants obtained in parametric optimization, all fibers, Yamashita-Kawabata model.

Constants	Aramid	HMPE	LC HMPE	LCP	PA	PET	HE PET
γ	0.500	0.500	0.500	0.500	0.497	0.500	0.500
τ	301.196	157.702	81.817	301.025	37.939	22.116	20.397
C_1	147.064	218.343	174.165	144.976	4.231	21.712	21.765
C_2	3.00×10^{-8}	0.664	3.451	3.00×10^{-8}	6.53×10^{-6}	2.04×10^{-4}	2.10×10^{-7}
C_3	1.304	1.000	1.066	1.609	2.949	2.962	5.018

Table H17. Constants obtained in parametric optimization, all fibers, Yeoh 2 terms model.

Constants	Aramid	HMPE	LC HMPE	LCP	PA	PET	HE PET
γ	0.500	0.500	0.500	0.500	0.500	0.500	0.500
τ	301.196	157.702	81.514	301.025	37.500	22.292	20.395
C_1	147.064	218.343	174.019	144.976	3.927	21.385	21.818
C_2	5.00×10^{-8}	0.332	1.922	1.70×10^{-7}	0.011	0.033	0.002

Table H18. Constants obtained in parametric optimization, all fibers, Yeoh 3 terms model.

Constants	Aramid	HMPE	LC HMPE	LCP	PA	PET	HE PET
γ	0.500	0.500	0.500	0.500	0.500	0.500	0.500
τ	301.196	157.702	81.891	301.025	36.157	22.120	20.398
C_1	147.064	218.343	174.173	144.976	4.162	21.607	21.746
C_2	1.10×10^{-7}	0.332	1.638	1.50×10^{-7}	1.81×10^{-6}	3.00×10^{-7}	4.00×10^{-8}
C_3	4.00×10^{-8}	9.00×10^{-8}	0.048	4.00×10^{-8}	1.13×10^{-4}	0.001	2.76×10^{-4}

Table H19. Constants obtained in parametric optimization, all fibers, Yeoh 5 terms model.

Constants	Aramid	HMPE	LC HMPE	LCP	PA	PET	HE PET
γ	0.500	0.500	0.500	0.500	0.450	0.500	0.500
τ	301.196	157.702	82.200	301.025	38.655	22.117	20.399
C_1	147.064	218.343	174.250	144.976	4.217	21.715	21.754
C_2	1.10×10^{-7}	0.332	1.601	3.00×10^{-8}	2.30×10^{-7}	9.00×10^{-8}	$< 1.00 \times 10^{-8}$
C_3	2.00×10^{-8}	6.50×10^{-6}	2.16×10^{-6}	1.00×10^{-8}	8.17×10^{-6}	3.00×10^{-8}	$< 1.00 \times 10^{-8}$
C_4	$< 1.00 \times 10^{-8}$	1.46×10^{-6}	5.90×10^{-7}	$< 1.00 \times 10^{-8}$	1.19×10^{-6}	4.56×10^{-5}	$< 1.00 \times 10^{-8}$
C_5	2.00×10^{-8}	4.90×10^{-7}	0.003	2.00×10^{-8}	$< 1.00 \times 10^{-8}$	2.00×10^{-8}	7.30×10^{-7}

Table H20. Constants obtained in parametric optimization, all fibers, Yeoh Modified model.

Constants	Aramid	HMPE	LC HMPE	LCP	PA	PET	HE PET
γ	0.500	0.500	0.492	0.499	0.500	0.500	0.500
τ	310.015	157.702	81.892	305.386	25.121	20.091	17.907
C_1	6.081	81.702	78.296	0.013	3.220	20.571	20.695
C_2	0.014	0.337	2.119	4.97×10^{-5}	0.020	0.068	0.051
C_3	0.246	2.60×10^{-7}	0.046	5.40×10^{-7}	9.10×10^{-7}	4.00×10^{-8}	1.00×10^{-8}
C_4	146.026	136.640	95.877	147.724	2.666	3.600	5.199
C_5	0.046	7.53×10^{-5}	0.010	0.017	0.230	0.836	0.918

ORCID iD

Daniel Magalhães da Cruz https://orcid.org/0000-0001-8734-0371
Felipe Tempel Stumpf https://orcid.org/0000-0002-8767-9516
Jakson Manfredini Vassoler https://orcid.org/0000-0002-8548-8935

How to cite this article: da Cruz D.M., Stumpf, F.T., Vassoler J.M. Comparative Assessment of Hyperelastic Models for Simulating Mechanical Hysteresis in Synthetic Yarns for Offshore Mooring, *J. Appl. Comput. Mech.*, xx(x), 2026, 1–23. https://doi.org/10.22055/jacm.2026.49306.5879